HCF101 is a novel component of the CIA cytosolic iron-sulfur synthesis pathway in the human pathogen *Toxoplasma gondii*

Eléa A. Renaud[1], Ambre J.M. Maupin[1], Laurence Berry[1], Julie Bals[2], Yann Bordat[1], Vincent Demolombe[2], Valérie Rofidal[2], Florence Vignols[2] and Sébastien Besteiro[1*]

[1]*LPHI, Univ. Montpellier, CNRS, INSERM, France;* [2]*IPSiM, Univ. Montpellier, CNRS, INRAE, Institut Agro, France*

*correspondance : *sebastien.besteiro@inserm.fr*

Abstract

Several key cellular functions depend on proteins harboring an iron-sulfur (Fe-S) cofactor. As these Fe-S proteins localize to several subcellular compartments, they require a dedicated machinery for cofactor assembly. For instance, in plants and algae there are Fe-S cluster synthesis pathways localizing to the cytosol, but also present in the mitochondrion and in the chloroplast, two organelles of endosymbiotic origin. *Toxoplasma gondii* is a plastid-bearing parasitic protist responsible for a pathology affecting humans and other warm-blooded vertebrates. We have characterized the *Toxoplasma* homologue of HCF101, originally identified in plants as a protein transferring Fe-S clusters to photosystem I subunits in the chloroplast. Contrarily to plants, we have shown that HCF101 does not localize to the plastid in parasites, but instead is an important component of the cytosolic Fe-S assembly (CIA) pathway which is vital for *Toxoplasma*. While the CIA pathway is widely conserved in eukaryotes, it is the first time the involvement of HCF101 in this pan-eukaryotic machinery is established. Moreover, as this protein is essential for parasite viability and absent from its mammalian hosts, it constitutes a novel and promising potential drug target.

Introduction

Iron-sulfur (Fe-S) clusters are ancient inorganic cofactors of proteins which are essential in virtually all forms of life [1]. These cofactors are found in a variety of proteins involved in numerous electron transfer and metabolic reactions that support key housekeeping cellular functions like respiration, photosynthesis, DNA repair and replication, protein translation, RNA modifications, but also in regulatory proteins and environmental signals sensors [2,3]. The most common clusters, which in most Fe-S proteins function as electron transfer groups [4], are in the rhombic [2Fe-2S], cubane [4Fe-4S], or more rarely the intermediate [3Fe-4S] configuration. Assembly of these cofactors is a carefully controlled process in order to avoid cellular toxicity arising from the accumulation of free Fe and S, which are highly reactive. Different Fe-S cluster assembly pathways developed early in evolution to synthesize the clusters and can be found in archaea, bacteria, and then evolved to mitochondrial, plastidic and cytosolic iron-sulfur assembly machineries in eukaryotes [5,6]. Thus, eukaryotic Fe-S cluster assembly machineries found in organelles of endosymbiotic origin were inherited from Alphaproteobacteria (the 'iron sulfur cluster', or ISC, pathway in the mitochondrion) and Cyanobacteria (the 'sulfur mobilization', or SUF, pathway in plastids), while a specific machinery ('cytosolic iron-sulfur cluster assembly', or CIA) is used for the biogenesis of cytosolic and nuclear Fe-S proteins.

While the individual components of these Fe-S assembly machineries display some structural diversity, they involve similar biochemical steps [7]. Typically, a cysteine desulfurase will generate sulfur from L-cysteine, scaffold proteins and chaperones will provide a molecular platform allowing the assembly of Fe and S into a cluster, and finally carrier proteins will deliver the cluster to target apoproteins. This happens in a similar fashion but with a specific molecular machinery in the three subcellular compartments in which Fe-S cluster synthesis takes place in eukaryotes, with a main difference that the early step of CIA depends on the mitochondrial machinery. In fact, although de novo cluster assembly has been suggested to happen in the cytosol of mammalian cells [8], experimental evidence in a large variety of eukaryotes points to the requirement of mitochondrial ISC components, in particular the Nfs1 cysteine desulfurase, to generate a S precursor that will be translocated to the cytosol [9–11]. In mammals and yeast, P-loop NTPases NUBP1 and NUBP2 are the scaffolds for initial [4Fe-4S] Fe-S cluster assembly in the CIA system [12] and electrons are provided by DRE2, together with NDOR1 (ATR3 in plants) [13]. Noticeably, some eukaryotes like plants lack a NUBP2 homologue and the scaffolding complex is instead composed of a dimer of NBP35, the NUBP1 homologue [14]. NAR1, a protein containing two [4Fe-4S] clusters, then acts as the Fe-S carrier and associates with the CIA targeting complex (CTC) [15]. The CTC, that will recognize client apoproteins through direct interactions and mediate the insertion of the Fe-S cluster, typically comprises MET18/MMS19 (plant/human nomenclature), CIA1/CIAO1, and AE7/CIAO2B [16].

Toxoplasma gondii is a widespread obligate intracellular parasitic protist belonging to the phylum Apicomplexa. Infection is usually harmless to immunocompetent individuals, but can lead to severe life-threatening disease in developing fetuses and immunocompromised individuals [17]. This parasite contains two organelles of endosymbiotic origin: a mitochondrion and a relict plastid called apicoplast, which are both of high metabolic importance [18]. Consequently, like in plants and algae *T. gondii* harbors three distinct Fe-S cluster synthesis pathways: the CIA in the cytosol, ISC in the mitochondrion and SUF in the apicoplast [19–21]. The SUF pathway being essential for the survival of the parasite and absent from its mammalian host, its components and client proteins are particularly attractive as potential drug targets [22], which prompted us to look for Fe-S proteins absent from mammals but present in plant and apicomplexan parasites. Investigating the Fe-S cluster assembly components in

68 protists, which are highly divergent phylogenetically from the canonical yeast or mammalian cell
69 models, can bring interesting insights into the evolution of this molecular machinery [23,24].

70 Here, we report the characterization of the *T. gondii* homologue of the high-chlorophyll-fluorescence
71 101 (HCF101) protein, which is typically a plastid-associated Fe-S transfer protein in the plant
72 *Arabidopsis thaliana* [25,26]. Our work shows that TgHCF101 is essential for parasite viability and we
73 demonstrate for the first time its implication in the eukaryotic CIA pathway.

74

75 Results

76 *TgHCF101 is a cytosolic protein*

77 HCF101 is a putative P-loop containing nucleoside triphosphate hydrolase that belongs to the
78 Mrp/NBP35 family (also called ApbC) of dimeric iron-sulfur carrier proteins that are found ubiquitously
79 in all domains of life and thus likely appeared early during evolution [27,28]. Compared with NBP35, in
80 addition to the nucleotide hydrolase domain HCF101 also contains a N-terminal DUF59/MIP18-family
81 domain [29], as well as a C-terminal domain of unknown function (DUF971). We performed homology
82 searches in the http://www.ToxoDB.org database to retrieve members of the Mrp/NPB35 family
83 encoded by the *T. gondii* genome. Besides TgNBP35, that has an unusual mitochondrial localization in
84 *T. gondii* [20,24], in line with previous studies [24,30] we identified TGGT1_318590 as a potential
85 homologue of HCF101. A broader phylogenetic analysis that included members of the Mrp/NPB35
86 family from a wide variety of eukaryotes (S1 Table), revealed that this putative *T. gondii* homologue
87 clearly segregates with members of the HCF101 group, clearly distinct from NBP35 homologues (Fig.
88 1A). Moreover, its primary sequence analysis confirmed a three domain-organization typical of HCF101
89 proteins, while NBP35 homologues mostly consist of the central ATPase domain (Fig. 1B). Of note, our
90 analysis, in accordance with a previous study [24], confirmed the absence of a CFD1 homologue in
91 Apicomplexa, contrarily to what has been suggested by a recent report [31]. In conclusion,
92 TGGT1_318590 may be named TgHCF101.

93 In *A. thaliana*, the *HCF101* mutant was found to be impaired in photosynthesis [32]: interfering with
94 HCF101 function has an impact on the maturation of both photosystem I (PSI) and ferredoxin-
95 thioredoxin reductases, which contain [4Fe-4S] clusters [25,26]. The apicoplast harbored by
96 apicomplexan parasites has lost the ability to perform photosynthesis [33], and some members of the
97 Apicomplexa phylum, like *Cryptosporidium*, have even completely lost the plastid [34] while it has
98 retained a HCF101 homologue (Fig. 1A, S1 Fig.). Thus, a function linked to photosystem seems unlikely
99 for apicomplexan parasites. Sequence analysis confirmed that, in contrast to plant homologues,
100 TgHCF101 lacks a predicted N-terminal transit peptide, which is typically needed for plastid import (Fig.
101 1B). Interestingly, *Chromera velia*, a close non-parasitic relative of Apicomplexa whose plastid has
102 retained its photosynthetic capacity [35], has two HCF101 isoforms: one with a predicted transit
103 peptide (thus potentially addressed to the plastid), and one without (Fig. 1, S1 Fig.). Specific analysis
104 of selected eukaryotic HCF101 homologs showed that Apicomplexa proteins, like ciliates and
105 dinoflagellates, form distinct groups that are clearly separate from the Archaeplastida group of plants
106 and algae bearing plastid-associated HCF101 isoforms (S1 Fig.). Interestingly, while the transit peptide-
107 bearing *C. velia* isoform segregates with homologs of plastid-containing eukaryotes, the second
108 isoform is closer to the Apicomplexa homologs (S1 Fig.). A recent study suggests that the plastid-
109 located HCF101 likely evolved from an ancestral cytosolic version of the protein [24]. This led us to
110 hypothesize that apicomplexan HCF101 would be involved in a cytosolic-related, rather than in a
111 plastid-associated, Fe-S cluster transport function.

112 To assess experimentally the localization of TgHCF101, we first tagged an ectopic copy with a C-
113 terminal GFP and observed a cytosolic localization (S2A Fig.), in line with what had been described
114 previously when an additional copy of TgHCF101 bearing a C-terminal Human influenza hemagglutinin
115 (HA) tag was expressed [24]. However, a stable TgHCF101-GFP cell line could not be established,
116 suggesting the potential importance of C-terminal accessibility for proper protein function. We then
117 next generated a transgenic cell line in which we modified the 5' region of the *TgHCF101* gene by
118 homologous recombination to replace the endogenous promoter by an inducible-Tet07*SAG4*
119 promoter, and at the same time adding a sequence coding for a N-terminal hemagglutinin (HA) tag
120 (Fig. 1C, D). In this conditional knock-down (cKD) HA-TgHCF101 cell line, the addition of
121 anhydrotetracycline (ATc) can repress transcription of *TgHCF101* through a Tet-Off system [36]. Two
122 independent transgenic clones were obtained and found to behave similarly in the initial phenotypic
123 assays we performed, so only one will be described in details here.

124 Immunoblot analysis showed a N-terminal HA-tagged protein at around 70 kDa (the predicted
125 molecular mass for TgHCF101), and depletion of the protein was efficient upon addition of ATc (Fig.
126 1E). Immunofluorescence assay (IFA) showed a punctate cytosolic signal for TgHCF101, clearly distinct
127 from the apicoplast, and efficiently depleted by the addition of ATc (Fig. 1F). Disruption of the
128 apicoplast-located SUF pathway has a strong impact on the lipoylation of the E2 subunit of the
129 pyruvate dehydrogenase (PDH-E2) by Fe-S-containing lipoate synthase LipA [19,22]. However,
130 depletion of TgHCF101 did not seem to have an impact on the lipoylation profile of PDH-E2 (S2B Fig.).
131 Disruption of the SUF pathway also typically impacts the apicoplast-located isoprenoid synthesis,
132 which involves two Fe-S oxidoreductases (IspG and IspH) and has been shown to have downstream
133 consequences on the glycosylation of proteins involved in parasite motility [22]. We thus assessed the
134 gliding motility of the parasites after TgHCF101 depletion and found that it was only affected after four
135 days of ATc treatment, which might be reflecting long-term impact of TgHCF101 depletion on parasite
136 fitness rather than a direct consequence of apicoplast-related Fe-S cluster synthesis (S3A, B Fig.).

137 Altogether, our results indicate that TgHCF101 is not associated with the apicoplast-located SUF
138 pathway, but localizes to the cytosol instead.

139

140 *TgHCF101 is essential for parasite growth*

141 We next assessed the impact of TgHCF101 depletion on the parasite's lytic cycle: we evaluated the
142 capacity of TgHCF101-depleted tachyzoites (a highly replicative and highly invasive form responsible
143 for the acute form of the disease caused by *T. gondii*) to generate lysis plaques. For this, we infected a
144 monolayer of host cells in absence or continuous presence of ATc for 7 days (Fig. 2A, B). Depletion of
145 TgHCF101 completely prevented plaque formation. While absence of plaques highlights a fitness
146 problem for the parasites, it does not necessarily implies their death: for instance, in response to stress,
147 tachyzoites can convert into a slow-growing and cyst-enclosed persisting stage called bradyzoites
148 (associated with the chronic form of the disease), that can reactivate when they encounter more
149 favourable conditions [37]. We thus performed a similar experiment, in which the ATc was washed out
150 at the end of the 7-day incubation, and then incubated the parasites for an extra 7 days in the absence
151 or presence of ATc before evaluating plaque formation (Fig. 2C). We did not observe any plaques after
152 ATc removal, suggesting that the parasites were not able to recover after 7 days of TgHCF101
153 depletion, likely because they were dead.

154 To assess whether this defect in the lytic cycle is due to a replication problem, cKD HA-TgHCF101
155 parasites were preincubated in ATc for 48 hours and then released mechanically, before infecting new
156 host cells for an additional 24 hours in ATc prior to parasite counting. We noted that incubation with

157 ATc led to an accumulation of vacuoles with fewer parasites (Fig. 2D). To get more precise insights into
158 the impact of TgHCF101 depletion on parasite division, we labeled dividing parasites with inner
159 membrane complex (IMC) protein IMC3 [38] to detect growing daughter cells (Fig. 2E). *T. gondii*
160 tachyzoites develop inside a mother cell by a process called endodyogeny [39] and this division is
161 usually highly synchronous within the same parasitophorous vacuole, yet after two days of ATc
162 treatment vacuoles showed a marked lack of synchronicity for daughter cell budding (Fig. 2E).
163 Investigation of the consequences of TgHCF101 depletion on developing parasites by electron
164 microscopy highlighted important defects on cytokinesis, including incomplete daughter cell budding
165 or defaults in organellar segregation (Fig. 2F, S4 Fig.). We also observed occasional vacuoles and
166 cytoplasmic clefts (Fig. 2F, S4 Fig.). However, the overall appearance of organelles seemed essentially
167 normal (Fig. 2F, S4 Fig.). To get a more general overview, we performed IFA using organelle-specific
168 markers, which confirmed that TgHCF101 depletion leads to defaults in the replication or segregation
169 of organelles, some daughter cells appearing devoid of apicoplast, mitochondrial or nuclear material
170 (S5 Fig.). Finally, through propidium iodide labeling and flow cytometer-based analysis of DNA content,
171 we observed that long-term depletion of TgHCF101 led to the emergence of an increasing
172 subpopulation of parasites with sub-1N DNA content, thus smaller than the typical haploid 1N DNA
173 content of the parasites (Fig. 2G), suggesting an impairment in DNA synthesis.

174 Overall, our results indicate that TgHCF101 depletion leads to important and, apparently, irreversible
175 defects in parasite replication and growth.

176

177 *Depletion of TgHCF101 induces stress response mechanisms*

178 Through electron microscopy analysis, we also noticed that the depletion of TgHCF101 induced the
179 appearance of structures resembling lipid droplets (LDs) in several parasites (Fig. 3A, S4 Fig.). In order
180 to properly quantify this, we used Nile red, a selective fluorescent stain for neutral lipids, and
181 microscopic imaging (Fig. 3B). We noticed a strong increase in both the number and size of LD in cKD
182 HA-TgHCF101 parasites incubated for two days with ATc (Fig. 3C, D). To see if this was a common
183 feature induced by abolishing Fe-S synthesis, we quantified LDs in mutants of the mitochondrial
184 (TgISU1) and apicoplast (TgSUFC) pathways [19]. Depletion of these proteins did not lead to an increase
185 in LD formation (S6A and B Fig.), indicating that LD induction may be linked to a pathway distinct from
186 the mitochondrial or plastid-related Fe-S cluster assembly machinery. We then also tested a recently
187 characterized mutant for TgABCB7L (a mitochondrial transporter of a sulfur precursor upstream of the
188 CIA pathway [40]) and a mutant of the CIA shuttle protein TgNAR1 (www.ToxoDB.org entry
189 TGGT1_242580) that we generated, and which is important for parasite fitness (S7 Fig.). Interestingly,
190 both these CIA-related mutants induced an increase in LD numbers (although more modest for the
191 TgABCB7L mutant), while only the TgNAR1 led to a statistically significant increase in LD size (Fig. 3C,
192 D).

193 As LD droplet induction seems to be a feature common to CIA pathway mutants and to the TgHCF101
194 mutant, we thought that TgHCF101 may play a role in this pathway. Additional supporting evidence
195 comes from the characterization of a C-terminal targeting complex recognition (TCR) signal ending with
196 an aromatic residue ([LIM]-[DES]-[WF]) in the clients proteins of the cytosolic Fe-S cluster machinery
197 or their adaptors [41], which can be clearly identified in the apicomplexan HCF101 homologues (Fig.
198 4A). Of note, this motif is also present in the *C. velia* isoform that has no transit peptide and thus which
199 is likely to have a plastid-independent function (Fig. 4A). Importantly, the last three amino acids of
200 TgHCF101 (LEW, Fig. 4A) constitute a canonical TCR motif. Thus, from the cKD HA-TgHCF101 mutant,
201 we generated cell lines in which we expressed either a wild-type copy or one deleted for this putative

202 TCR signal (Fig. 4B, C). As expected, expression of these additional copies was unaltered by ATc
203 treatment (Fig. 4D), and the corresponding proteins localized to the cytoplasm (Fig. 4E). Upon
204 depletion of the ATc-regulated copy, expressing the extra wild-type copy was efficient in restoring
205 parasite growth (Fig. 4F, G) and preventing LD accumulation (Fig. 4H, I). Yet, in sharp contrast,
206 expressing the TCR-deleted extra copy did not improve parasite fitness (Fig. 4F, G) and did not prevent
207 induction of LD formation (Fig. 4H, I).

208 To assess if the induction of LD formation could play a role in the demise of the parasites, we used
209 T863, a pharmaceutical inhibitor of the acyl coenzyme A:diacylglycerol acyltransferase 1 (DGAT1)
210 enzyme, which is important for storing neutral lipids in cytoplasmic LD [42]. While treatment with T863
211 efficiently decreased the number of LDs (S6C, D and E Fig.), long term incubation during plaque assays
212 did not allow any recovery in parasite fitness (S6F Fig.). This suggests that LDs are not detrimental to
213 TgHCF101-depleted parasites (or at least not solely responsible for their demise), but instead could be
214 part of an integrated stress response, as they have been shown in other eukaryotes to be upregulated
215 in response to cellular injuries including nutrient-related and oxidative stresses [43].

216 Disrupting proteins involved in Fe-S cluster assembly may have a direct effect on the stability and
217 expression levels of local Fe-S proteins. Thus, to get insights into the effect of TgHCF101 depletion at
218 the molecular level, we performed global label-free quantitative proteomic analyses. Of course, this
219 may also affect downstream cellular pathways or functions, and other pathways may also be
220 upregulated in compensation. cKD HA-TgHCF101 or TATi ΔKu80 parental control parasites were
221 treated for three days with ATc prior to a global proteomic analysis and compared for protein
222 expression. We selected candidates with a $\log_2$(fold change) ≤-0.55 or ≥0.55 (corresponding to a ~1.47-
223 fold change in decreased or increased expression) and a p-value <0.05 (ANOVA, *n*=4 biological
224 replicates) and we completed this dataset by selecting some candidates that were consistently and
225 specifically absent from the mutant cell lines or only expressed in these (S2 and S3 Tables). Many
226 proteins with higher abundance were bradyzoite stage-specific and more particularly components of
227 the cyst wall or their cell surface [44,45] (Fig. 5A, B, S2 Table). Tachyzoites can convert to the persistent
228 bradyzoite form upon stress, so to verify if TgHCF101 depletion was inducing stage conversion we used
229 a lectin from the plant *Dolichos biflorus*, which recognizes the SRS44/CST1 cyst wall glycoprotein in
230 differentiating cysts [46] (Fig. 5C, D). We could see that TgHCF101 depletion induced the appearance
231 of up to 10% of lectin-labeled vacuoles during the first 48 hours of intracellular growth in the presence
232 of ATc. However, when parasites were kept for up to a week in the presence of ATc, the proportion of
233 lectin-positive vacuoles plateaued at 14%, and only a very limited number of vacuoles looked like bona
234 fide mature cysts (less than 2% were both lectin-positive and containing more than 2 parasites) (Fig.
235 5E).

236 These data suggest that depletion of TgHCF101 leads to a cellular stress that initiates stage conversion
237 into the bradyzoite stage, but that the differentiation process into mature cysts cannot be completed.

238

239 *Depletion of TgHCF101 affects specifically cytosolic and nuclear Fe-S proteins*

240 The label-free quantitative proteomic analyses also highlighted proteins which were less expressed in
241 absence of TgHCF101. Among them, were a surprisingly large number of rhoptry bulb proteins (S3
242 Table, S8A Fig.). Rhoptries are club-shaped organelles that comprise a narrow tubular neck opening at
243 the anterior pole of the parasite, and a most posterior bulbous part; the proteins secreted from these
244 different sub-compartments are either involved in invasion and parasitophorous vacuole formation,
245 or in the modulation of host cell defenses, respectively [47]. We assessed if there was any major impact
246 of TgHCF101 depletion on rhoptry morphology or function. We performed IFA with anti-armadillo

247 repeats only protein (TgARO), a protein homogenously anchored to the surface of the rhoptry
248 membrane [48], and found no particular defect in rhoptry morphology or positioning (S8B Fig.), in
249 accordance with our initial electron microscopy analysis (Fig. 2F). Quantification of intracellular
250 evacuoles (rhoptry-secreted vesicular clusters) did not indicate any particular problem in the secretory
251 capacity of the organelles upon TgHCF101 depletion (S8C Fig.). Finally, we assessed by immunoblot the
252 expression profile of one of the potentially less-expressed rhoptry bulb protein but found only a slight
253 alteration in the expression profile (a modest increase in the non-mature from of the protein), but not
254 in the overall amount of protein (S8D Fig.). We conclude that although TgHCF101 depletion may lead
255 to a secondary impact on rhoptry content, it does not extensively impact organelle morphology or
256 secretory function.

257 Given the potential implication of TgHCF101 in the biogenesis of Fe-S proteins, we also specifically
258 searched for putative Fe-S proteins in the less expressed proteins highlighted by the label-free
259 quantitative proteomic analysis. We have previously estimated the Fe-S proteome using a
260 computational predicting metal-binding sites in protein sequences [49], which, coupled with the data
261 from global mapping of *T. gondii* proteins subcellular location by HyperLOPIT spatial proteomics [50],
262 allows predicting client proteins present in the mitochondrion, apicoplast or cytosol [19]. We found
263 three Fe-S proteins that were less expressed upon TgHCF101 depletion (Fig. 5A). Interestingly, they
264 were all connected to the CIA pathway as they were NAR1, a Fe-S carrier to the CIA core machinery
265 [15], and two Fe-S proteins depending on the CIA machinery for their maturation [51]: ABCE1 (Rli1 in
266 yeast), a cytosolic ribosomal recycling factor and NTHL1, a nuclear DNA base-excision repair enzyme.
267 In order to verify the proteomics data, we tagged TgABCE1 with a myc epitope in the context of the
268 cKD HA-TgHCF101 mutant (S9A and B Fig.). IFA showed a decrease in the cytosolic TgABCE1 signal (Fig.
269 5B), which was supported by quantitative immunoblot analysis indicating a statistically significant
270 decrease in TgABCE1 upon treatment of cKD HA-TgHCF101 mutant with ATc (Fig. 5C, D).

271 We did not manage to tag TgNTHL1 to verify if its abundance was effectively affected by TgHCF101
272 depletion. The catalytic subunit of DNA polymerase delta (TgPOLD1), which is another nucleus-
273 associated Fe-S protein, was found to be decreasing in abundance in the CIA-related TgABCB7L mutant
274 [40]. Our quantitative proteomic analysis did not highlight a particular decrease in TgPOLD1 abundance
275 upon TgHCF101 depletion: it was found to be stable, or even slightly more abundant (by a 1.4-fold),
276 after two days of TgHCF101 depletion. Yet, we knew it could be tagged and decided to use this to
277 investigate more thoroughly a potential global impact TgHCF101 depletion on nuclear and cytoplasmic
278 Fe-S proteins. We thus created a conditional knockdown line of TgHCF101 in the POLD1-HA
279 background [40] and verified that it displayed a similar phenotype to the original cKD HA-TgHCF101
280 cell line (S10 Fig.). In the TgABCB7L mutant, TgPOLD1 abundance was found to be sharply decreasing
281 early, before any noticeable impact on TgABCE1 [40]. In contrast, upon TgHCF101 depletion we
282 observed a limited and delayed decrease in TgPOLD1 abundance (Fig. 6E, F, G) and intriguingly,
283 TgPOLD1 levels even seemed to increase in the first two days of TgHCF101 depletion (Fig. 6F, G). This
284 is in sharp contrast with the more rapid and complete impact on TgABCE1 (Fig. 6B, C, D). Of note, IFAs
285 highlighted that although TgHCF101 depletion did not lead to a marked loss of TgPOLD1, in some
286 parasites the protein remained in the cytoplasm instead of being translocated to the nucleus (Fig. 6E),
287 which in fact corresponds to a stage where we have shown that DNA content of the parasite is affected
288 (Fig. 2G).

289 These results indicate that while perturbing TgHCF101 expression potentially has consequences on
290 several proteins associated with the CIA machinery, it may be more specifically important for the
291 maturation of the TgABCE1 cytosolic Fe-S protein.

292

293 *TgHCF101 is likely a Fe-S transfer protein of the CIA complex.*

294 To get further insights on the role played by TgHCF101 in the CIA machinery, we next performed co-
295 immunoprecipitations (co-IPs) and mass spectrometry identification of associated proteins, comparing
296 lysates of cKD HA-TgHCF101 parasites grown in the presence of ATc or not (S4 Table). Strikingly, we
297 pulled-down all three *T. gondii* homologues of the core components of the CTC: MET18, CIA1 and AE7
298 (a MIP18 family protein) (Fig. 7A). We managed to tag the TgCIA1 protein with a myc epitope tag in
299 the context of the HA-tagged TgHCF101 cell line (S9C and D Fig.) and performed a reverse IP by which
300 we managed to specifically pull-down TgHCF101, confirming their interaction (Fig. 7B). It should be
301 noted that this result was only obtained when this experiment was performed after chemical
302 crosslinking, suggesting a possibly indirect or transient interaction between the proteins.

303 Another interesting candidate that was found co-immunoprecipitated with TgHCF101 was TgABCE1,
304 strengthening the possibility of an important relationship between the two proteins. We next
305 performed a reverse IP and could recover small amounts of TgHCF101 co-eluting specifically with
306 TgABCE1 (Fig. 7C). To further investigate this potential interaction, we performed yeast two-hybrid
307 assay, based on interaction-dependent transactivation of the *HIS3* reporter gene (Fig. 7D). This
308 experiment confirmed that there is a direct interaction between TgHCF101 and TgABCE1, and
309 highlighted a particularly strong interaction, as it was retained when using 3-aminotriazole, a
310 competitive inhibitor of the *HIS3* gene product (Fig. 7D). While this confirms that TgABCE1 is likely a
311 client protein of TgHCF101, we could not confirm a direct interaction between TgHCF101 and TgNTHL1
312 using the same method (S11 Fig.). Given the known implication of ABCE1 in translation, we next
313 evaluated the impact of TgHCF101 depletion on translation by using a puromycin-based assay (Fig. 7E).
314 Puromycin can mimic aminoacyl-tRNA and becomes covalently attached to nascent peptides, thereby
315 allowing the evaluation of protein elongation rates with an anti-puromycin antibody [52]. Using this
316 method, we could show that TgHCF101 depletion leads to a modest but a statistically significant
317 decrease in the overall translation rate (Fig. 7E, F).

318 Together, these results suggest that TgHCF101 acts as a Fe-S transfer protein to the translation
319 regulator TgABCE1.

320

321 Discussion

322 Fe-S clusters are universal among living organisms, where they play key roles in many important
323 biological processes as cofactors of proteins involved for instance in housekeeping functions like
324 respiration, photosynthesis, as well as genome expression or maintenance [6]. These cofactors were
325 acquired early during evolution, and thus they played a fundamental role in the evolution of the
326 eukaryotic cells as they were inherited through endosymbiosis to organelles such as the mitochondrion
327 or plastids [5]. Different Fe-S cluster synthesis pathways show globally-conserved mechanistic and
328 biochemical features to assemble and transfer the clusters prior to transferring them to client proteins
329 [7]. However, beyond a core Fe-S synthesizing machinery, given the large diversity of eukaryotic
330 lineages, it is likely that some have evolved some specific features.

331 For instance proteins of the MRP/NBP35 family (NBP35, Cfd1, Ind1 and HCF101), have in common a
332 central P-loop NTPase domain [27], but are either involved in scaffolding or transfer of Fe-S clusters at
333 specific subcellular locations like the mitochondrion, the plastid, or in the cytosol [12,25,26,53].
334 Presence of MRP family members in bacteria that are able to bind Fe-S clusters point to ancient and
335 conserved function linked to Fe-S biogenesis for these proteins [54]. Another feature shared by

336 members of this family is their ability to form homo- or hetero-dimers bridging one Fe-S cluster at their
337 interface through two conserved and functionally essential Cys residues [55]. Interestingly, HCF101
338 also presents at its N-terminal a MIP18-like domain that constitutes most of a bacterial protein called
339 SufT that is involved in Fe-S maturation [29,54,56], as well as a C-terminal domain whose function is
340 not yet defined (DUF971). The presence of additional domain besides the conserved NTPase core
341 domain in members of the MRP family like HCF101 suggests that they may have additional or more
342 specialized functions. Another clue of evolutionary specialization comes from the different localization
343 of protein isoforms in different species, hinting for a possible association to different Fe-S cluster
344 biogenesis machineries. A recent study suggested a wide diversity in localization for HCF101 paralogs
345 across eukaryotes, with isoforms potentially localizing to the mitochondrion in *Tetrahymena* or in the
346 cytosol in *T. gondii* [24]. More precisely, in some chromalveolates a mitochondrial HCF101 isoform
347 likely replaced Ind1 for the maturation of Fe-S subunits of the complex I of the mitochondrial electron
348 transport chain. Yet, as *T. gondii* lacks complex I, it has no Ind1 homolog and no particular need for a
349 mitochondrion-located HCF101 isoform either. Moreover, while HCF101 was initially characterized as
350 a chloroplast-associated protein with a specialized function in maintaining PSI homeostasis, our study
351 confirms that although *T. gondii* harbors a plastid, TgHCF101 is expressed in the cytosol (Fig. 1F, S2A
352 Fig.), which is consistent with the absence of photosynthesis-related pathways in *T. gondii*. Our study
353 establishes for the first time that the cytosolic expression of TgHCF101 is functionally related to the
354 CIA pathway (Fig. 8).

355 Previous functional investigations of the CIA pathway in *T. gondii* focused on TgABCB7L, a
356 mitochondrial transporter presumably involved in providing a sulfur-containing precursor for further
357 processing by the cytosolic Fe-S assembly machinery [40] and on TgNBP35, a Fe-S scaffolding protein
358 of the CIA that displays an unusual association with the outer mitochondrial membrane in the parasites
359 [20]. The mitochondrial localization of these proteins, which are quite upstream in the CIA machinery,
360 suggests that the assembly of cytosolic Fe-S clusters likely happens at the cytosolic face of the
361 mitochondrion in *T. gondii*, and then probably shuttle through the *T. gondii* NAR1 homologue to the
362 CTC for subsequent transfer to client proteins (Fig. 8). CTC proteins have so far not been functionally
363 investigated in the parasite, but both TgABCB7L and TgNBP35 are essential for parasite growth and
364 were both shown to be important for TgABCE1 stability [20,40]. The TgNAR1 mutant that we generated
365 in this study also shows that this CIA shuttle protein is essential for parasite fitness (S7D Fig.).
366 Combining genome-wide data for potential essentiality and localization [50,57] to metal-binding site
367 prediction algorithms [49], our previous assessment of the putative *T. gondii* cytosolic and nuclear Fe-
368 S proteome highlighted proteins involved in key functions like genome reparation and maintenance,
369 mRNA synthesis and protein expression [19]. It is thus unsurprising to see that *T. gondii* mutants of the
370 CIA pathway are severely impaired in growth. Our quantitative proteomics analysis of the TgHCF101
371 mutant did not reveal an impact on a large number of nuclear or cytosolic Fe-S proteins, which may
372 indicate that this protein could be involved in cluster transfer to a reduced subset of Fe-S proteins.
373 Besides the decrease in abundance of TgNAR1, strengthening the evidence of TgHCF101 involvement
374 in the CIA pathway, quantitative proteomics data revealed a decrease in two potential client Fe-S
375 proteins: TgABCE1 and TgNTHL1. While we could establish a direct association of TgHCF101 with
376 TgABCE1 by co-immunoprecipitations and yeast two-hybrid (Fig. 7A, C, D), we did not manage to tag
377 TgNTHL1 to perform co-immunoprecipitations and we did not obtain proof of a direct
378 TgHCF101/TgNTHL1 interaction by yeast two-hybrid. Besides, when we tested the impact of TgHCF101
379 depletion on TgPOLD1, a Fe-S protein known to be affected by the disruption of the CIA pathway [40],
380 we saw a limited and delayed effect compared with the one we observed on TgABCE1 (Fig. 6). Whether
381 or not TgHCF101 is able to transfer clusters to Fe-S proteins besides TgABCE1 is still an open question,
382 yet, so far, the evidence we gathered points primarily to TgABCE1 as its main client protein.

383 Our phenotypic analysis of TgHCF101-depleted parasites revealed cell division and DNA replication
384 problems (Fig. 2D, G) that might result from an impact on Fe-S protein-mediated DNA maintenance,
385 but may also be secondary (and more general) effects of TgHCF101 depletion. In addition, through
386 perturbation of TgABCE1 function, we measured a decrease in the overall translation rate in the
387 parasites (Fig. 7E, F), that could contribute to their decreased fitness and growth problems. Upon two
388 days of TgHCF101 depletion, parasites also started to display an accumulation of LDs (Fig. 3). LDs are
389 known to be induced as part of an integrated stress response to cellular injuries and may be induced
390 in conditions such as oxidative stress [43]. For instance, during the particular Fe-induced cell death
391 called ferroptosis, iron excess combined to oxygen leads to the accumulation of reactive oxygen
392 species (ROS). This leads to subsequent peroxidation of lipids, which in turn induces the accumulation
393 of lipid droplets that act as antioxidant organelles to control polyunsaturated fatty acid storage in
394 triglycerides in order to reduce membrane lipid peroxidation [58]. Although it is possible that
395 perturbation of the CIA pathway created local imbalance in cytosolic Fe concentration and ROS-
396 dependent stress that contributed to the demise of the parasites, it is to note that our previous work
397 has shown that general Fe deprivation has a similar LD-inducing effect on the parasites [59]. So,
398 altogether, this may rather suggest that specific CIA-dependent Fe-S protein(s) that remain to be
399 identified could be involved in regulating LDs. Even more so than the induction of LDs, initiation of
400 stage conversion to the bradyzoite persistence form is a hallmark of the stress response in *T. gondii*
401 [37]. Upon depletion of TgHCF101 we could detect early signs of differentiation (Fig. 5), but the
402 parasites were largely unable to progress to full stage conversion and died instead (Fig. 2C, Fig. 5E).
403 Importantly, overall our data show that TgHCF101 is essential for parasite viability, and although our
404 findings point towards an involvement of this protein in the eukaryote-conserved CIA pathway, its
405 specific absence from the mammalian hosts of the parasite makes it a good potential drug target. This
406 calls for further structure/function studies of TgHCF101 in order to potentially design specific
407 inhibitors.

408 There is a vast repertoire of Fe-S client proteins with a diverse range of structures and roles, and one
409 important conundrum remaining in the Fe-S research field is resolving functional specificity of the
410 transfer proteins during the addition of Fe-S to apoproteins. Key investigations in budding yeast
411 allowed the identification of mutually exclusive sub-complexes of the CTC that can transfer Fe-S
412 clusters to different proteins [51,60]. In particular, it was shown that a complex of two small proteins,
413 Yae1 and Lto1, functions as a target-specific adaptor to recruit the yeast homologue of ABCE1 (called
414 Rli1) to the generic CIA machinery [60]. These adaptor proteins are well-conserved in phylogenetically-
415 close opisthokonts like humans, in which they have also been shown to be important for ABCE1
416 maturation [61,62]. However, Yae1 and Lto1 are clearly not conserved across all eukaryotes but found
417 essentially in fungi, metazoan and plants (S12 Fig.), and thus noticeably they do not seem to have
418 homologues in the Alveolata superphylum that includes apicomplexan parasites. So, while ABCE1 is
419 arguably one of the most conserved proteins in evolution and is universally present in all eukaryotes
420 [63], the factors driving its CIA-dependent maturation seem phylogenetically divergent. We have now
421 established that in *T. gondii*, HCF101 is associated to the CTC and likely plays that role in this organism.
422 Given sequence conservation of HCF101 homologs, it is also likely to be the case in other apicomplexan
423 parasites and even possibly in one isoform present in the photosynthetic relative *C. velia* (Fig. 1A, B,
424 S1 Fig.). Our results highlight the complex evolutionary adaptation that accompanied the maturation
425 of eukaryotic Fe-S proteins and calls for in-depth structural analysis of this interaction. Not only this
426 would provide invaluable evolutionary insights into the molecular machinery supporting Fe-S cluster
427 transfer, but also may provide new prospects for interfering specifically with an essential function as a
428 new strategy against apicomplexan-caused diseases.

429

Materials and methods

Cell culture

Toxoplasma gondii RH tachyzoites and derived transgenic cell lines generated in this study were routinely maintained through passages in human foreskin fibroblasts (HFFs) monolayer (ATCC CRL-1634). HFFs and parasites were cultured in standard Dulbecco's Modified Eagle's Medium (DMEM, supplemented with 5% decomplemented fetal bovine serum (FBS), 2 mM L-glutamine, 100 U/mL penicillin and 100 µg/mL streptomycin (Gibco) in a controlled atmosphere at 37°C and with 5% CO_2.
For immunoprecipitation assays, parasites were grown in Vero cells (ATCC, CCL-81) in the same conditions as for the HFFs.
Transgenic cell lines were generated in the TATi ΔKu80 genetic background line lacking the *Ku80* gene and expressing the TATi transactivator required for the TetOff system [64]. For positive selection of transgenic parasites bearing resistance cassettes for expressing dihydrofolate reductase thymidylate synthase (DHFR-TS) or chloramphenicol acetyltransferase (CAT) were grown with 1 µM pyrimethamine or 20 µM chloramphenicol (Sigma-Aldrich, SML3579, C0378), respectively. Conditional depletion in the TetOff conditional knockdown lines was achieved by incubation with 0,5 µg/mL anhydrotetracycline (ATc, Fluka 37919) for the indicated duration of the assay.

Bioinformatic analyses

Genomic and protein sequences were retrieved from http://www.toxodb.org or https://www.ncbi.nlm.nih.gov/protein/. Protein alignments were performed from eukaryotic MRP family proteins (S1 Table), whose sequences were obtained from Grosche et al. [65], and updated by manual curation. Iterative rounds of alignment were performed with MAFFT v.7.475 using the E-INF-i refinement method (adapted for several conserved motifs that are embedded in long unalignable regions) https://mafft.cbrc.jp/alignment/server/index.html [66]. Sequence trimming and optimization was then performed with BMGE v.1.12 (https://ngphylogeny.fr/tools/tool/273/form) [67], with a minimal block size of 1. A phylogeny was then inferred from this dataset by maximum likelihood using the IQ-TREE software v.2.1.2 (http://www.iqtree.org/) [68], with 1,000 ultrafast bootstrap replicates [69]. Phylogenetic trees were rendered using the MEGA software v.11.0.13 (https://www.megasoftware.net/) [70] or with iTOL (https://itol.embl.de/) [71].
Transit peptide and subcellular localization predictions were performed using the ChloroP 1.1 (https://services.healthtech.dtu.dk/services/ChloroP-1.1/), IPSORT (http://ipsort.hgc.jp/), and Localizer 1.0.4 (http://localizer.csiro.au/) algorithms. Domain searches were performed using the Interpro database (https://www.ebi.ac.uk/interpro/).

Generating a GFP-tagged TgHCF101 cell line

cDNA corresponding to the *TgHCF101* gene (TGGT1_318590) was amplified by PCR with primers ML4715 and ML4716 (all primers used in the present study are listed in S5 Table) and sub-cloned using XhoI and KpnI into the pEZS-NL vector (D. Ehrhardt, https://deepgreen.dpb.carnegiescience.edu/cell%20imaging%20site%20/html/vectors.html) for a C-terminal GFP fusion. The TgHCF101-GFP cassette was them amplified by PCR using the ML4817 and ML4818 primers and cloned using BclI and EcoRV in a BglII/EcorV-digested pTUB-IMC1-TdT vector [72] to drive the expression from a tubulin promoter. Tachyzoites were transfected with 100 µg of plasmid and observed by fluorescence microsocopy.

Generating a conditional TgHCF101 knock-down cell line

To generate the construct for the tetracycline-regulated conditional depletion of TgHCF101 and add a N-terminal HA tag, we digested the DHFR-TetO7Sag4 plasmid [72] by BglII and inserted a fragment coding for a single HA tag generated through hybridization of the ML4924 and ML4925 oligonucleotides. Then, a 1,066 bp fragment corresponding to the 5' coding part of TgHCF101 was

480 amplified by PCR with primers ML4926 and ML4927 and inserted after digesting with BglII and NotI, to
481 yield the DHFR-TetO7Sag4-HA-TgHCF101 plasmid. The TATi ΔKu80 cell line was transfected with 80 µg
482 of the BsiWI-linearized plasmid. Transgenic parasites, named cKD HA-TgHCF101, were selected with
483 pyrimethamine and cloned by limiting dilution. Positive clones were verified by PCR with primers
484 ML1771 and ML6043.
485
486 *Generating complemented cell lines*
487 The cKD TgHCF101-HA cell line was complemented by adding an extra copy of the *TgHCF101* gene
488 under the control of a tubulin promoter at the *UPRT* locus. The entire *TgHCF101* cDNA sequence (1935
489 bp) was amplified by PCR using primers ML6409/ML6410 from the plasmid pGBKT7-myc-HCF101 to
490 express a N-terminal myc-tagged HCF101 copy. This sequence was then cloned downstream of the
491 tubulin promoter in the pUPRT-TUB vector [64], resulting in the pUPRT-myc-TgHCF101 plasmid. The
492 plasmid was subsequently linearized prior to transfecting the mutant cell line, together with a plasmid
493 expressing Cas9 and a *UPRT*-specific guide RNA under the control of a U6 promoter [73]. Transgenic
494 parasites were selected using 5 µM 5-fluorodeoxyuridine (Sigma-Aldrich) and cloned by serial limiting
495 dilution to obtain the cKD TgHCF101 WT complemented cell line.
496 For complementation with the copy of TgHCF101 lacking the LEW tripeptide motif, the cDNA sequence
497 was amplified by PCR using primers ML6409/ML6412 from the plasmid pGADT7-myc-HCF101, to
498 remove the tripeptide motif in the C-terminal region. All constructs were verified by sequencing.
499 Cloning and transfection were performed as previously described to establish the cKD TgHCF101 -LEW
500 comp cell line. For both cell lines correct integration at the *UPRT* locus was verified by PCR using
501 primers ML6044 and ML6396.
502
503 *Generating a conditional TgNAR1 knock-down cell line*
504 We digested the DHFR-TetO7Sag4 plasmid by BglII and then, a fragment corresponding to the 5' coding
505 part of *TgNAR1* was amplified by PCR with primers ML5862 and ML5863 and inserted after digesting
506 with BamHI and NotI to yield the DHFR-TetO7Sag4-TgNAR1 plasmid. The TATi ΔKu80 cell line was
507 transfected with 80 µg of the NsiI-linearized plasmid. Transgenic parasites, named cKD HA-TgNAR1,
508 were selected with pyrimethamine and cloned by limiting dilution. Positive clones were verified by PCR
509 with primers ML1771 and ML5947.
510
511 *Tagging of ABCE1 and CIA1 in the TgHCF101 knock-down background*
512 A CRISPR-based strategy was used to C-terminally tag proteins of interest in the cKD HA-TgHCF101
513 background. Guide RNAs (gRNAs) targeting the C-terminal end of the gene of interest were selected
514 using CHOP-CHOP tool (https://chopchop.cbu.uib.no/). gRNAs were cloned into the pU6-Cas9
515 Universal Plasmid (Addgene, 52694) using BsaI. Donor DNA was amplified by PCR using the high fidelity
516 KOD DNA polymerase (Novagen) to amplify a fragment containing the tag and the resistance cassette,
517 using the pLIC-myc-CAT plasmid as a template, adding at both ends 30-nucleotide overhangs
518 homologous to the C-terminal region of the gene of interest for homologous recombination. *TgABCE1*
519 (TGGT1_216790) tagging was performed by using primers ML5126 and ML5127 for the gRNA and
520 ML5128 and ML5129 to amplify donor DNA, yielding the cKD HA-TgHCF101 TgABCE1-myc cell line.
521 Integration of the construct was controlled by PCR using GoTaq DNA polymerase (Promega) with
522 primers ML6115 and ML4310. *TgCIA1* (TGGT1_313280) tagging was performed by using primers
523 ML5932 and ML5933 for the gRNA and ML5934 and ML5935 to amplify donor DNA, yielding the cKD
524 HA-TgHCF101 TgCIA1-myc cell line. Integration of the construct was controlled by PCR using GoTaq
525 DNA polymerase (Promega) with primers ML5936 and ML4310.
526
527 *Generating a TgHCF101 knock-down cell line with HA-tagged POLD1*
528 The POLD1-HA cell line [40] was used as a background to generate a tetracycline-regulated conditional
529 TgHCF101 mutant. Primers ML4926 and ML4927 were used to amplify a a 1,066 bp 5' fragment of the
530 *TgHCF101* coding sequence and cloned using BglII/NotI in the DHFR-TetO7Sag4 plasmid [72] to yield
531 the DHFR-TetO7Sag4-TgHCF101 plasmid. The POLD1-HA cell line was transfected with 80 µg of this

532 plasmid linearized by NsiI. Transgenic parasites were selected with pyrimethamine and cloned by
533 limiting dilution. Positive clones were verified by PCR with primers ML2456 and ML6043.
534
535 *Semi-quantitative RT-PCR*
536 Semi-quantitative RT-PCR was performed as described previously [74]. Briefly, 1µg of RNA was used as
537 a template for each RT-PCR reaction and specific primers for *TgHCF101* (ML5112/ML5113), *TgNAR1*
538 (ML6467/ML6468) or *TUB2* (Tubulin β chain) (ML841/ML842) were used. Twenty-four cycles of PCR
539 were performed.
540
541 *Immunofluorescence assays*
542 For immunofluorescence assays (IFA), coverslips seeded with HFFs were infected by *T. gondii*
543 tachyzoites. Intracellular parasites and host cell monolayer were then fixed with 4% (w/v)
544 paraformaldehyde (PFA, diluted in phosphate-buffered saline -PBS-) for 20 minutes. After fixation, cells
545 were permeabilized with 0.3% (v/v) Triton X-100 (diluted in PBS) for 10 minutes. Coverslips were
546 blocked with 2% (w/v) bovine serum albumin (BSA) for 1h prior to immunolabeling with primary
547 antibody for 1 hour. After 3 washes in PBS, corresponding secondary antibody was incubated for 1
548 hour. Coverslips were finally incubated with 1 µg/mL 4,6-diamidino-2-phenylindole (DAPI) for 5
549 minutes before 3 washes in PBS and, lastly, mounted using Immu-Mount (ThermoFisher) onto
550 microscope slides. Primary antibodies used were prepared in 2% BSA (diluted in PBS) and used at the
551 following concentrations: rat monoclonal anti-HA (1:1000, 3F10 Roche), mouse monoclonal anti-myc
552 (1:100, 9E10 Sigma), rabbit anti-IMC3 (1:1000) [75], mouse anti-SAG1 (T41E5, 1:1000) [76], rabbit anti-
553 armadillo repeats only (ARO, 1:1000) [48], rabbit anti-PDH-E2 (1:500) [22], mouse anti-F1β ATPAse
554 (1:1000, gift of P. Bradley). Cysts were stained with biotin labeled *Dolichos Biflorus* lectin (1:300, Sigma
555 L-6533) and detected with FITC-conjugated streptavidin (1:300, Invitrogen, SNN1008). Lipid droplets
556 were detected with Nile Red (1 µg/mL, Sigma 72485), using the CY3/DsRed BP550/25 FT570 BP605/70
557 filter cube (Zeiss) on an epifluorescence microscope.
558 All images were acquired at the Montpellier Ressources Imagerie (MRI) facility. Observations were
559 performed with Zeiss AxioImager Z1 and Z2 epifluorescence microscopes equipped with a Zeiss
560 Axiocam MRm CCD camera and 63X/1.4 or 100X/1.4 Oil Plan Achromat objective. Images were
561 processed on Zen Blue v3.6 (Blue edition) software (Zeiss). Z-stack acquisitions were processed by
562 maximum intensity orthogonal projection when assessing lipid droplets number and area. Adjustments
563 of brightness and contrast were applied uniformly and paired images were acquired with the same
564 exposure time.
565
566 *Plaque and replication assays*
567 The lytic cycle of tachyzoites was assessed by plaque assay as described previously [59]. Briefly,
568 tachyzoites from the cKD HA-TgHCF101 transgenic cell line or parental strain (TATi ΔKu80) were
569 allowed to invade monolayers of HFFs in the presence or absence of ATc. Parasites were cultivated for
570 7 days at 37°C and 5% CO_2 and fixed with 4% (w/v) PFA (diluted in PBS) for 20 minutes. Cells were
571 stained with 0.1% crystal violet solution (V5265, Sigma-Aldrich), washed and air-dried before imaging
572 on an Olympus MVX10 microscope. For the reversibility assay, drug washout was carefully performed
573 after 7 days of ATc pre-treatment and cultures were kept for another 7 days of growth, non-treated
574 control conditions were also infected at this timepoint.
575 For replication assay, parasites were pre-treated in flasks for 48 hours with ATc and extracellular
576 parasites were allowed to invade HFF monolayer on coverslips for another 24 hours before being fixed
577 and performing parasites immunodetection by IFA with mouse anti-SAG1 antibody as described
578 before. The number of parasites per vacuole was scored. Independent experiments were conducted
579 three times, and 200 random vacuoles were counted for each condition.
580
581 *Immunoblotting and antibodies*
582 Protein extracts were prepared from 10^7 extracellular parasites resuspended in Laemmli buffer at a
583 final concentration of 10^6 parasites/µL. Extracts were treated with benzonase to remove DNA from

584 samples and resolved by SDS-PAGE before being transferred on nitrocellulose membrane for
585 subsequent protein detection. Primary antibodies used for immunodetection were resuspended at
586 their respective working concentration in 5% (w/v) milk in TNT buffer (0.1 M Tris-HCl, pH 7.6, 0.15 M
587 NaCl, 0.05%, Tween 20). Antibodies used in this study for immunoblot detection were rat anti-HA
588 (1:1000, Roche), mouse anti-myc (1:100, Sigma), mouse anti-SAG1 (1:50, hybridoma), mouse anti-actin
589 (1:25, hybridoma) [77], mouse anti-ROP7 (1:1000, T43H1) [78], mouse anti-puromycin (1:1000,12D10,
590 MABE943 Sigma) and rabbit anti-lipoic acid (1:500, ab58724 Abcam) [79].
591
592 *Puromycin labeling*
593 Strains of interest were grown for 3 days in the presence or absence of ATc. Freshly egressed parasites
594 were filtered on 40µm Cell Strainer (VWR, 723-2757). After filtration and counting, parasites were
595 treated with puromycin (100 µg/mL, puromycin dihydrochloride, Sigma) for 15 minutes at 37°C and
596 5% CO_2. For translation inhibition control, parasites were treated with cycloheximide (100 µg/mL,
597 Sigma) for 10 minutes prior to puromycin incubation. After treatment, parasites were washed in DPBS
598 (Dulbecco's phosphate-buffered saline, Gibco) and collected by centrifugation. Pellet was resuspended
599 in Laemmli buffer and separated on Mini-Protean TGX Stain-free gels 12% (BioRad) activated by a UV-
600 induced 1-minute reaction to produce tryptophan residue fluorescence in order to allow for global
601 protein quantification, following manufacturer instructions. Proteins were then transferred to
602 nitrocellulose membrane for immunodetection using mouse anti-puromycin (1:1000,12D10, MABE943
603 Sigma) and mouse anti-actin (1:25, hybridoma). Total protein content is assessed by Stain-free
604 detection and puromycin signal is detected with secondary antibody mouse coupled with alkaline
605 phosphatase. Both signals were quantified by densitometry using the ImageJ software.
606
607 *Electron microscopy*
608 Parasites were pretreated with ATc for 48h and allowed to reinvade for 24h in the presence of ATc.
609 Untreated parasites were used as a control for normal morphology. Cells were then fixed with 2.5%
610 glutaraldehyde in cacodylate buffer 0.1 M pH7.4. Coverslips were subsequently processed using a
611 Pelco Biowave pro+ (Ted Pella). Samples were postfixed in 1% OsO4 and 2% uranyl acetate, dehydrated
612 in acetonitrile series and embedded in Epon 118 using the following parameters: Glutaraldehyde (150
613 W ON/OFF/ON 1-min cycles); two buffer washes (40 s 150 W); OsO4 (150 W ON/OFF/ON/OFF/ON 1-
614 min cycles); two water washes (40 s 150 W); uranyl acetate (100 W ON/OFF/ON 1-min cycles);
615 dehydration (40 s 150 W); resin infiltration (350 W 3-min cycles). Fixation and infiltration steps were
616 performed under vacuum. Polymerization was performed at 60°C for 48 hr. Ultrathin sections at 70
617 nM were cut with a Leica UC7 ultramicrotome, counterstained with uranyl acetate and lead citrate and
618 observed in a Jeol 1400+ transmission electron microscope from the MEA Montpellier Electron
619 Microscopy Platform. All chemicals were from Electron Microscopy Sciences, and solvents were from
620 Sigma.
621
622 *Label-free quantitative proteomics*
623 Parasites from the TATi ΔKu80 and cKD HA-TgHCF101 cell lines were treated for 72 hours in HFF seeded
624 in T75 cm^2 flasks. After suitable incubation, parasites were released from host cells with a cell scraper
625 and passed through a 25G needle before filtration on a fiber glass wool column. Parasites were pelleted
626 and washed in Hank's Balanced Salt Solution (HBSS, Gibco). Parasites were resuspended in lysis buffer
627 (1% SDS, 50mM Tris HCL pH 8, 10mM EDTA pH 8) and protein quantification was determined with the
628 bicinchoninic acid kit (Abcam). For each condition, 20 µg of protein resuspended in Laemmli buffer
629 were resolved on a 10% SDS-PAGE for 35 minutes at 100V. Proteins were fixed with a combination of
630 acetic acid and ethanol and stained in PageBlue Protein Staining Solution (ThermoScientific). Each lane
631 was cut in three identical pieces which were digested with trypsin and peptide extraction was done as
632 previously described [80].
633 LC-MS/MS experiments were performed using an Ultimate 3000 RSLC nano system (ThermoFisher)
634 interfaced online with a nano easy ion source and an Exploris 240 Plus Orbitrap mass spectrometer
635 (ThermoFisher). The .raw files were analyzed with MaxQuant version 2.0.3.0 using default settings

636 (PMID: 19029910). The minimal peptide length was set to 6. The files were searched against the *T.*
637 *gondii* proteome (March 2020, https://www.uniprot.org/proteomes/UP000005641-8450). Identified
638 proteins were filtered according to the following criteria: at least two different trypsin peptides with
639 at least one unique peptide, an E value below 0.01 and a protein E value smaller than 0.01 were
640 required. Using the above criteria, the rate of false peptide sequence assignment and false protein
641 identification were lower than 1%. Proteins were quantified by label-free method with MaxQuant
642 software using unique and razor peptides intensities [81]. Statistical analyses were carried out using
643 RStudio package software. The protein intensity ratio (protein intensity in mutant/protein intensity in
644 parent) and statistical tests were applied to identify the significant differences in the protein
645 abundance. Hits were retained if they were quantified in at least three of the four replicates in at least
646 one experiment. Proteins with a statistically significant ($p < 0.05$ or 0.01 with or without Benjamini
647 correction) quantitative ratio were considered as significantly up-regulated and down-regulated
648 respectively. Volcano plots were generated with the Perseus software v2.0.7.0
649 (https://maxquant.net/perseus/). Perseus was also used for hierarchical clustering of bradyzoite- and
650 tachyzoite-specific surface antigens of the SRS family using RNAseq data of Hehl et al. [82], available
651 on www.Toxodb.org.
652
653 *Co-immunoprecipitation and mass spectrometry identification*
654 Parasites of the cKD HA-TgHCF101 transgenic cell line were treated for 3 days in the presence or
655 absence of ATc in T175 cm^2 seeded with Vero cells. After treatment, intracellular parasites were
656 released by scraping of the host cells and three passages through a 26G needle. To eliminate cell host
657 debris, parasites were filtered through fiber glass wool and harvested by centrifugation at 650g for 5
658 min and washed three times in DPBS (Gibco). Parasites were resuspended in lysis buffer (1%NP40, 50
659 mM Tris-HCl pH8, 150 mM NaCl, 4 mM EDTA, supplemented with cOmplete Mini protease inhibitors
660 mix (Roche)) and incubated overnight at 4°C on a rotating wheel. Centrifugation of insoluble material
661 was performed at 13500g for 30 min at 4°C. The supernatant was transferred to a tube containing 50µL
662 of anti-HA magnetic beads (ThermoFisher, 88836) for 4h at 4°C on a rotating wheel. The depleted
663 fraction was then removed and beads were washed 5 times with lysis buffer. For the elution of
664 immunoprecipitated proteins, beads were incubated in 50 µL of HA peptide solution at 2 mg/mL
665 (ThermoFisher, 26184) for 1h at 37°C on a rotating wheel. The eluted proteins were mixed with
666 Laemmli buffer and resolved on a 10% SDS-Page for 35 minutes at 100V. In-gel proteins were fixed
667 with a combination of acetic acid and ethanol and stained with PageBlue Protein Staining Solution
668 (ThermoScientific). Each lane was cut in three identical pieces which were digested with trypsin,
669 peptide extraction was done as previously described [80] and mass spectrometry identification was
670 performed as described for label-free quantitative proteomic.
671 Proteomic data were analyzed on R following the publicly available script of DEP analysis package
672 (https://github.com/arnesmits/DEP, v.1.7.1). The following parameters were used for differential
673 expression analysis: dataset was normalized by variance-stabilizing transformation and missing values
674 were imputed via MNAR (missing not at random) method, the fold change cutoff was set at 1.5 and p-
675 value at 0.05. Statistical analyses were performed by a differential enrichment test based on protein-
676 wise linear models and empirical Bayes statistics [83] and p-values were adjusted by the Benjamini-
677 Hochberg correction.
678 Validation of co-immunoprecipitation mass spectrometry results was performed by immunoblotting.
679 C-terminally c-myc tagged candidates in the cKD HA-TgHC101 background were grown in the presence
680 or absence of ATc for 48h. Parasites were harvested and subjected to co-immunoprecipitation using
681 myc-Trap agarose beads (Chromotek, yta-20) following manufacturer's instructions. Cross-linking of
682 proteins was performed prior to co-immunoprecipitation for the cKD HA-TgHCF101 CIA1-myc cell line
683 using 1% (w/v) PFA (diluted in PBS) for 5 minutes at room temperature and quenched with 125 mM
684 ice-cold glycine. Immunoprecipitated proteins were then resolved on 10% SDS-Page prior to
685 immunoblot analysis.
686
687 *Yeast two-hybrid*

688 RNA was extracted from parasites using NuceloSpin RNA kit (Macherey-Nagel). cDNA was obtained
689 using SuperScript III First Strand Synthesis SuperMix for RT-qPCR (Invitrogen) using oligodT and
690 following the manufacturer's instructions. Specific cDNAs were subsequently amplified using KOD DNA
691 polymerase (Novagen). Cloning was performed with In-Fusion HD cloning kit (Takara) for each
692 candidate into pGADT7 and pGBKT7 vectors (Clontech, Takara Bio) to allow expression of AD-(Gal4
693 activation domain) and BD-(Gal4 DNA binding domain) fusion proteins, respectively. Primers were
694 designed using the InFusion Cloning Primer Design Tool (https://takarabio.com/) and are listed in S5
695 Table.
696 All experiments were performed in the Gal4-based yeast two-hybrid (Y2H) reporter strain YRG2
697 (MATα, *ura3-52*, *his3-200*, *ade2-101*, *lys2-801*, *leu2-3*, *112*, *trp1-901*, *gal4-542*, *gal80-538*,
698 *lys2*::UAS_{GAL1}-$TATA_{GAL1}$-HIS3, URA3::$UAS_{GAL4,17MERS(x3)}$-$TATA_{CYC1}$-LacZ) (Stratagene, Agilent). Yeast cells
699 were co-transformed by pGAD/pGBK construct pairs and selected on plates containing the minimal
700 YNB medium (0.7% Yeast Nitrogen Base medium without amino acids, 2% glucose, 2% Difco agar)
701 supplemented with histidine (H), adenine (A), Lysine (K), and uracil (U) according to Gietz and Woods
702 [84]. For all Y2H interaction assays, individual co-transformed colonies were cultured on liquid
703 YNB+HUKA, adjusted to an OD_{600} of 0.05 and dotted on YNB+UKA plates containing (+His plates) or
704 missing (-His plates) histidine (7 µL per dot). Plates were incubated at 30°C, and cell growth was
705 recorded after 5 days. Constructs pairs including empty vectors (AD-fusion + empty BD, or empty AD +
706 BD-fusion) were tested first to evaluate the capacity of each protein of interest to transactivate the
707 *HIS3* reporter gene in the absence of interactor, and to determine the appropriate 3-aminotriazole
708 (3AT) concentration required to abolish false interactions. True positive interactions were visualized
709 as cells growing on YNB+UKA in the absence of histidine (-his plates) and eventually in the presence of
710 3AT if required. Increasing 3AT concentrations were also used to challenge the strength of positive
711 interactions. For all assays, at least three independent transformations per construct pair were
712 performed.
713
714 *DNA content analysis*
715 DNA content analysis by flow cytometry was performed as described previously [85]. Parasites from
716 the cKD HA-TgHCF101 strain and from the background line TATi ΔKu80 were treated for up to four days
717 in the presence or absence of ATc. Extracellular parasites were removed by washing with HBSS and
718 intracellular parasites were released from host cell by scraping with a cell scraper (VWR, 734-2602),
719 passages through 26G needles and finally filtered on a fiber glass wool column. Parasites were then
720 fixed overnight in a solution of 70% ethanol and 30% PBS at 4°C. After fixation, parasites were washed
721 in PBS and stained with a 30 µM propidium iodide solution for 30 min. Parasites DNA content was then
722 analyzed by flow cytometry with an Aurora cytometer (Cytek) from the MRI facility.
723
724 *Gliding motility assay*
725 Parasites from the parental TATi ΔKu80 and the cKD HA-TgHCF101 transgenic cell lines were grown in
726 the presence or absence of ATc for up to 4 days. 1.10^6 freshly egressed parasites were harvested and
727 resuspended in 400µL motility buffer (155 mM NaCl, 3 mM KCl, 2 mM $CaCl_2$, 1 mM $MgCl_2$, 3 mM
728 NaH_2PO_4, 10 mM HEPES, 10 mM glucose) and 100 µL of the suspension was immediately placed on
729 poly-L-lysine coated slides and incubated at 37°C for 15 min. Unattached parasites were removed by
730 performing three washes with PBS. Finally, attached parasites were fixed with 4% (w/v) PFA and
731 stained with anti-SAG1 antibody. Trails length (at least 100 per condition) were captured on random
732 fields with a 63x objective on a Zeiss AXIO Imager Z2 epifluorescence microscope and were quantified
733 using the NeuronJ plug-in on the ImageJ software as described previously [86].
734
735 *Rhoptry secretion assay*
736 Rhoptry secretion was quantified by performing an evacuole assay [87]. Parasites from the cKD HA-
737 TgHCF101 strain and cKD TgARO strain were grown in the presence or absence of tetracycline for up
738 to 72 hours. Freshly egressed parasites were then pre-treated for 10 min in DMEM supplemented with
739 1 µM cytochalasin D (cytD), an inhibitor of actin polymerization. Parasites were allowed to secrete

740 their rhoptry content as they were put in contact with HFF cells for 15 min in the presence of cytD at
741 37°C. Parasites and HFF cells were then immediately fixed with 8% (w/v, in PBS) PFA, permeabilized
742 with 0.1% Triton X-100 and stained with anti-ROP1 and anti-SAG1 to detect secreted rhoptry material
743 and parasites, respectively. For each technical replicate, 20 random fields were quantified and three
744 technical replicates were performed for each of the three biological replicates.
745
746 *Statistical analyses*
747 Statistical analyses were generally performed with the Prism 8.3 software (Graphpad). For proteomics
748 experiments, statistics were performed with version 4.2.1 of the R package (2022-06-23,
749 https://www.R-project.org/) using the Differential Enrichment analysis of Proteomics Data (DEP,
750 v.1.23.0) package. Unless specified, values are expressed as means ± standard deviation (SD).
751

752 # Data availability

753 All raw MS data and MaxQuant files generated have been deposited to the ProteomeXchange
754 Consortium via the PRIDE partner repository (https://www.ebi.ac.uk/pride/archive) with the dataset
755 identifiers PXD051549 and PXD051551.

756

757 # Acknowledgements

758 We thank B. Striepen, V. Carruthers, M.J. Gubbels, P. Bradley, A. MacLean and D. Soldati-Favre for the
759 gift of antibodies or cell lines. Mass spectrometry experiments were carried out using the facilities of
760 the Montpellier Proteomics Platform (PPM, MSPP site, BioCampus Montpellier), member of the
761 Proteomics French Infrastructure (ProFI). We also thank the developers and the managers of the
762 VeupathDB.org and ToxoDB.org databases, as well as scientists who contributed datasets. We
763 acknowledge the MRI Cell Imaging Facility, member of the national infrastructure France-BioImaging
764 for image acquisitions and cytometry analyses.

765

766 # Funding

767 This work was supported by the Agence Nationale de la Recherche (grant ANR-22-CE20-0026 to S.B.
768 and F.V.). The funders had no role in study design, data collection and analysis, decision to publish, or
769 preparation of the manuscript.

770

771 # References

772 1. Beinert H, Holm RH, Münck E. Iron-sulfur clusters: nature's modular, multipurpose structures.
773 Science. 1997;277: 653–659. doi:10.1126/science.277.5326.653

774 2. Andreini C, Putignano V, Rosato A, Banci L. The human iron-proteome. Metallomics. 2018;10:
775 1223–1231. doi:10.1039/c8mt00146d

776 3. Lill R, Freibert S-A. Mechanisms of mitochondrial iron-sulfur protein biogenesis. Annu Rev
777 Biochem. 2020;89: 471–499. doi:10.1146/annurev-biochem-013118-111540

778 4. Brzóska K, Meczyńska S, Kruszewski M. Iron-sulfur cluster proteins: electron transfer and
779 beyond. Acta Biochim Pol. 2006;53: 685–691.

780 5. Tsaousis AD. On the origin of Iron/Sulfur cluster biosynthesis in eukaryotes. Front Microbiol.
781 2019;10: 2478. doi:10.3389/fmicb.2019.02478

782 6. Garcia PS, D'Angelo F, Ollagnier De Choudens S, Dussouchaud M, Bouveret E, Gribaldo S, et al.
783 An early origin of iron–sulfur cluster biosynthesis machineries before Earth oxygenation. Nat
784 Ecol Evol. 2022;6: 1564–1572. doi:10.1038/s41559-022-01857-1

785 7. Braymer JJ, Freibert SA, Rakwalska-Bange M, Lill R. Mechanistic concepts of iron-sulfur protein
786 biogenesis in Biology. Biochimica et Biophysica Acta (BBA) - Molecular Cell Research.
787 2021;1868: 118863. doi:10.1016/j.bbamcr.2020.118863

788 8. Maio N, Rouault TA. Outlining the complex pathway of mammalian Fe-S cluster biogenesis.
789 Trends in Biochemical Sciences. 2020;45: 411–426. doi:10.1016/j.tibs.2020.02.001

790 9. Kispal G, Csere P, Prohl C, Lill R. The mitochondrial proteins Atm1p and Nfs1p are essential for
791 biogenesis of cytosolic Fe/S proteins. EMBO J. 1999;18: 3981–3989.
792 doi:10.1093/emboj/18.14.3981

793 10. Pondarré C, Antiochos BB, Campagna DR, Clarke SL, Greer EL, Deck KM, et al. The mitochondrial
794 ATP-binding cassette transporter Abcb7 is essential in mice and participates in cytosolic iron–
795 sulfur cluster biogenesis. Human Molecular Genetics. 2006;15: 953–964.
796 doi:10.1093/hmg/ddl012

797 11. Zuo J, Wu Z, Li Y, Shen Z, Feng X, Zhang M, et al. Mitochondrial ABC transporter ATM3 is
798 essential for cytosolic iron-sulfur cluster assembly. Plant Physiol. 2017;173: 2096–2109.
799 doi:10.1104/pp.16.01760

800 12. Camire EJ, Grossman JD, Thole GJ, Fleischman NM, Perlstein DL. The yeast Nbp35-Cfd1 cytosolic
801 iron-sulfur cluster scaffold is an ATPase. J Biol Chem. 2015;290: 23793–23802.
802 doi:10.1074/jbc.M115.667022

803 13. Netz DJA, Stümpfig M, Doré C, Mühlenhoff U, Pierik AJ, Lill R. Tah18 transfers electrons to Dre2
804 in cytosolic iron-sulfur protein biogenesis. Nat Chem Biol. 2010;6: 758–765.
805 doi:10.1038/nchembio.432

806 14. Kohbushi H, Nakai Y, Kikuchi S, Yabe T, Hori H, Nakai M. Arabidopsis cytosolic Nbp35
807 homodimer can assemble both [2Fe–2S] and [4Fe–4S] clusters in two distinct domains.
808 Biochemical and Biophysical Research Communications. 2009;378: 810–815.
809 doi:10.1016/j.bbrc.2008.11.138

810 15. Balk J, Pierik AJ, Netz DJA, Mühlenhoff U, Lill R. The hydrogenase-like Nar1p is essential for
811 maturation of cytosolic and nuclear iron-sulphur proteins. EMBO J. 2004;23: 2105–2115.
812 doi:10.1038/sj.emboj.7600216

813 16. Kassube SA, Thomä NH. Structural insights into Fe–S protein biogenesis by the CIA targeting
814 complex. Nat Struct Mol Biol. 2020;27: 735–742. doi:10.1038/s41594-020-0454-0

815 17. Sanchez SG, Besteiro S. The pathogenicity and virulence of Toxoplasma gondii. Virulence.
816 2021;12: 3095–3114. doi:10.1080/21505594.2021.2012346

817 18. Sheiner L, Vaidya AB, McFadden GI. The metabolic roles of the endosymbiotic organelles of
818 Toxoplasma and Plasmodium spp. Curr Opin Microbiol. 2013;16: 452–458.
819 doi:10.1016/j.mib.2013.07.003

820 19. Pamukcu S, Cerutti A, Bordat Y, Hem S, Rofidal V, Besteiro S. Differential contribution of two
821 organelles of endosymbiotic origin to iron-sulfur cluster synthesis and overall fitness in
822 Toxoplasma. Soldati-Favre D, editor. PLoS Pathog. 2021;17: e1010096.
823 doi:10.1371/journal.ppat.1010096

824 20. Aw YTV, Seidi A, Hayward JA, Lee J, Victor Makota F, Rug M, et al. A key cytosolic iron-sulfur
825 cluster synthesis protein localises to the mitochondrion of Toxoplasma gondii. Mol Microbiol.
826 2020; mmi.14651. doi:10.1111/mmi.14651

827 21. Renaud EA, Maupin AJM, Besteiro S. Iron-sulfur cluster biogenesis and function in Apicomplexa
828 parasites. Biochimica et Biophysica Acta (BBA) - Molecular Cell Research. 2025;1872: 119876.
829 doi:10.1016/j.bbamcr.2024.119876

830 22. Renaud EA, Pamukcu S, Cerutti A, Berry L, Lemaire-Vieille C, Yamaryo-Botté Y, et al. Disrupting
831 the plastidic iron-sulfur cluster biogenesis pathway in Toxoplasma gondii has pleiotropic effects
832 irreversibly impacting parasite viability. J Biol Chem. 2022;298: 102243.
833 doi:10.1016/j.jbc.2022.102243

834 23. Tsaousis AD, Gentekaki E, Eme L, Gaston D, Roger AJ. Evolution of the cytosolic iron-sulfur
835 cluster assembly machinery in Blastocystis species and other microbial eukaryotes. Eukaryot
836 Cell. 2014;13: 143–153. doi:10.1128/EC.00158-13

837 24. Pyrih J, Žárský V, Fellows JD, Grosche C, Wloga D, Striepen B, et al. The iron-sulfur scaffold
838 protein HCF101 unveils the complexity of organellar evolution in SAR, Haptista and Cryptista.
839 BMC Ecol Evol. 2021;21: 46. doi:10.1186/s12862-021-01777-x

840 25. Lezhneva L, Amann K, Meurer J. The universally conserved HCF101 protein is involved in
841 assembly of [4Fe-4S]-cluster-containing complexes in *Arabidopsis thaliana* chloroplasts. The
842 Plant Journal. 2004;37: 174–185. doi:10.1046/j.1365-313X.2003.01952.x

843 26. Schwenkert S, Netz DJA, Frazzon J, Pierik AJ, Bill E, Gross J, et al. Chloroplast HCF101 is a
844 scaffold protein for [4Fe-4S] cluster assembly. Biochem J. 2009;425: 207–214.
845 doi:10.1042/BJ20091290

846 27. Leipe DD, Wolf YI, Koonin EV, Aravind L. Classification and evolution of P-loop GTPases and
847 related ATPases. Journal of Molecular Biology. 2002;317: 41–72. doi:10.1006/jmbi.2001.5378

848 28. Boyd JM, Drevland RM, Downs DM, Graham DE. Archaeal ApbC/Nbp35 homologs function as
849 iron-sulfur cluster carrier proteins. J Bacteriol. 2009;191: 1490–1497. doi:10.1128/JB.01469-08

850 29. Mashruwala AA, Boyd JM. Investigating the role(s) of SufT and the domain of unknown function
851 59 (DUF59) in the maturation of iron–sulfur proteins. Curr Genet. 2018;64: 9–16.
852 doi:10.1007/s00294-017-0716-5

853 30. Seeber F, Soldati-Favre D. Metabolic pathways in the apicoplast of apicomplexa. International
854 Review of Cell and Molecular Biology. 2010. pp. 161–228.

855 31. Shrivastava D, Abboud E, Ramchandra JP, Jha A, Marq J-B, Chaurasia A, et al. ATM1, an essential
856 conserved transporter in Apicomplexa, bridges mitochondrial and cytosolic [Fe-S] biogenesis.
857 PLoS Pathog. 2024;20: e1012593. doi:10.1371/journal.ppat.1012593

858 32. Meurer J, Meierhoff K, Westhoff P. Isolation of high-chlorophyll-fluorescence mutants
859 ofArabidopsis thaliana and their characterisation by spectroscopy, immunoblotting and
860 Northern hybridisation. Planta. 1996;198: 385–396. doi:10.1007/BF00620055

861 33. Mathur V, Salomaki ED, Wakeman KC, Na I, Kwong WK, Kolisko M, et al. Reconstruction of
862 plastid proteomes of apicomplexans and close relatives reveals the major evolutionary
863 outcomes of cryptic plastids. Mol Biol Evol. 2023;40: msad002. doi:10.1093/molbev/msad002

864 34. Zhu G, Marchewka MJ, Keithly JS. Cryptosporidium parvum appears to lack a plastid genome.
865 Microbiology. 2000;146: 315–321. doi:10.1099/00221287-146-2-315

866 35. Moore RB, Oborník M, Janouskovec J, Chrudimský T, Vancová M, Green DH, et al. A
867 photosynthetic alveolate closely related to apicomplexan parasites. Nature. 2008;451: 959–
868 963. doi:10.1038/nature06635

869 36. Meissner M, Brecht S, Bujard H, Soldati D. Modulation of myosin A expression by a newly
870 established tetracycline repressor-based inducible system in Toxoplasma gondii. Nucleic Acids
871 Res. 2001;29: E115.

872 37. Cerutti A, Blanchard N, Besteiro S. The bradyzoite: a key developmental stage for the
873 persistence and pathogenesis of toxoplasmosis. Pathogens. 2020;9: 234.
874 doi:10.3390/pathogens9030234

875 38. Gubbels M-J, Wieffer M, Striepen B. Fluorescent protein tagging in Toxoplasma gondii:
876 identification of a novel inner membrane complex component conserved among Apicomplexa.
877 Molecular and Biochemical Parasitology. 2004;137: 99–110.
878 doi:10.1016/j.molbiopara.2004.05.007

879 39. Francia ME, Striepen B. Cell division in apicomplexan parasites. Nat Rev Microbiol. 2014;12:
880 125–136. doi:10.1038/nrmicro3184

881 40. Maclean AE, Sloan MA, Renaud EA, Argyle BE, Lewis WH, Ovciarikova J, et al. The Toxoplasma
882 gondii mitochondrial transporter ABCB7L is essential for the biogenesis of cytosolic and nuclear
883 iron-sulfur cluster proteins and cytosolic translation. Weiss LM, editor. mBio. 2024; e00872-24.
884 doi:10.1128/mbio.00872-24

885 41. Marquez MD, Greth C, Buzuk A, Liu Y, Blinn CM, Beller S, et al. Cytosolic iron–sulfur protein
886 assembly system identifies clients by a C-terminal tripeptide. Proc Natl Acad Sci USA. 2023;120:
887 e2311057120. doi:10.1073/pnas.2311057120

888 42. Nolan SJ, Romano JD, Kline JT, Coppens I. Novel approaches to kill Toxoplasma gondii by
889 exploiting the uncontrolled uptake of unsaturated fatty acids and vulnerability to lipid storage
890 inhibition of the parasite. Antimicrob Agents Chemother. 2018;62: e00347-18.
891 doi:10.1128/AAC.00347-18

892 43. Jarc E, Petan T. Lipid droplets and the management of cellular stress. Yale J Biol Med. 2019;92:
893 435–452.

894 44. Nadipuram SM, Thind AC, Rayatpisheh S, Wohlschlegel JA, Bradley PJ. Proximity biotinylation
895 reveals novel secreted dense granule proteins of Toxoplasma gondii bradyzoites. PLoS One.
896 2020;15: e0232552. doi:10.1371/journal.pone.0232552

897 45. Jung C, Lee CY-F, Grigg ME. The SRS superfamily of Toxoplasma surface proteins. International
898 Journal for Parasitology. 2004;34: 285–296. doi:10.1016/j.ijpara.2003.12.004

899 46. Tomita T, Bzik DJ, Ma YF, Fox BA, Markillie LM, Taylor RC, et al. The Toxoplasma gondii cyst wall
900 protein CST1 is critical for cyst wall integrity and promotes bradyzoite persistence. PLoS Pathog.
901 2013;9: e1003823. doi:10.1371/journal.ppat.1003823

902 47. Ben Chaabene R, Lentini G, Soldati-Favre D. Biogenesis and discharge of the rhoptries: Key
903 organelles for entry and hijack of host cells by the Apicomplexa. Mol Microbiol. 2021;115: 453–
904 465. doi:10.1111/mmi.14674

905 48. Mueller C, Klages N, Jacot D, Santos JM, Cabrera A, Gilberger TW, et al. The Toxoplasma protein
906 ARO mediates the apical positioning of rhoptry organelles, a prerequisite for host cell invasion.
907 Cell Host & Microbe. 2013;13: 289–301. doi:10.1016/j.chom.2013.02.001

908 49. Valasatava Y, Rosato A, Banci L, Andreini C. MetalPredator: a web server to predict iron-sulfur
909 cluster binding proteomes. Bioinformatics. 2016;32: 2850–2852.
910 doi:10.1093/bioinformatics/btw238

911 50. Barylyuk K, Koreny L, Ke H, Butterworth S, Crook OM, Lassadi I, et al. A comprehensive
912 subcellular atlas of the Toxoplasma proteome via hyperLOPIT provides spatial context for
913 protein functions. Cell Host & Microbe. 2020; S193131282030514X.
914 doi:10.1016/j.chom.2020.09.011

915 51. Stehling O, Mascarenhas J, Vashisht AA, Sheftel AD, Niggemeyer B, Rösser R, et al. Human
916 CIA2A-FAM96A and CIA2B-FAM96B integrate iron homeostasis and maturation of different
917 Subsets of cytosolic-nuclear iron-sulfur proteins. Cell Metabolism. 2013;18: 187–198.
918 doi:10.1016/j.cmet.2013.06.015

919 52. Schmidt EK, Clavarino G, Ceppi M, Pierre P. SUnSET, a nonradioactive method to monitor
920 protein synthesis. Nat Methods. 2009;6: 275–277. doi:10.1038/nmeth.1314

921 53. Bych K, Kerscher S, Netz DJA, Pierik AJ, Zwicker K, Huynen MA, et al. The iron–sulphur protein
922 Ind1 is required for effective complex I assembly. EMBO J. 2008;27: 1736–1746.
923 doi:10.1038/emboj.2008.98

924 54. Aubert C, Mandin P, Py B. Mrp and SufT, two bacterial homologs of eukaryotic CIA Factors
925 involved in Fe-S clusters biogenesis. Inorganics. 2023;11: 431. doi:10.3390/inorganics11110431

926 55. Stehling O, Jeoung J-H, Freibert SA, Paul VD, Bänfer S, Niggemeyer B, et al. Function and crystal
927 structure of the dimeric P-loop ATPase CFD1 coordinating an exposed [4Fe-4S] cluster for
928 transfer to apoproteins. Proc Natl Acad Sci U S A. 2018;115: E9085–E9094.
929 doi:10.1073/pnas.1807762115

930 56. Mashruwala AA, Bhatt S, Poudel S, Boyd ES, Boyd JM. The DUF59 containing protein SufT is
931 involved in the maturation of Iron-Sulfur (FeS) proteins during conditions of high FeS cofactor
932 demand in Staphylococcus aureus. PLoS Genet. 2016;12: e1006233.
933 doi:10.1371/journal.pgen.1006233

934 57. Sidik SM, Huet D, Ganesan SM, Huynh M-H, Wang T, Nasamu AS, et al. A Genome-wide CRISPR
935 Screen in Toxoplasma Identifies Essential Apicomplexan Genes. Cell. 2016;166: 1423-1435.e12.
936 doi:10.1016/j.cell.2016.08.019

937 58. Liang D, Minikes AM, Jiang X. Ferroptosis at the intersection of lipid metabolism and cellular
938 signaling. Molecular Cell. 2022;82: 2215–2227. doi:10.1016/j.molcel.2022.03.022

939 59. Renaud EA, Maupin AJM, Bordat Y, Graindorge A, Berry L, Besteiro S. Iron depletion has
940 different consequences on the growth and survival of Toxoplasma gondii strains. Virulence.
941 2024;15: 2329566. doi:10.1080/21505594.2024.2329566

942 60. Paul VD, Mühlenhoff U, Stümpfig M, Seebacher J, Kugler KG, Renicke C, et al. The deca-GX3
943 proteins Yae1-Lto1 function as adaptors recruiting the ABC protein Rli1 for iron-sulfur cluster
944 insertion. eLife. 2015;4: e08231. doi:10.7554/eLife.08231

945 61. Zhai C, Li Y, Mascarenhas C, Lin Q, Li K, Vyrides I, et al. The function of ORAOV1/LTO1, a gene
946 that is overexpressed frequently in cancer: essential roles in the function and biogenesis of the
947 ribosome. Oncogene. 2014;33: 484–494. doi:10.1038/onc.2012.604

948 62. Prusty NR, Camponeschi F, Ciofi-Baffoni S, Banci L. The human YAE1-ORAOV1 complex of the
949 cytosolic iron-sulfur protein assembly machinery binds a [4Fe-4S] cluster. Inorganica Chimica
950 Acta. 2021;518: 120252. doi:10.1016/j.ica.2021.120252

951 63. Navarro-Quiles C, Mateo-Bonmatí E, Micol JL. ABCE Proteins: From Molecules to development.
952 Front Plant Sci. 2018;9: 1125. doi:10.3389/fpls.2018.01125

953 64. Sheiner L, Demerly JL, Poulsen N, Beatty WL, Lucas O, Behnke MS, et al. A Systematic Screen to
954 Discover and Analyze Apicoplast Proteins Identifies a Conserved and Essential Protein Import
955 Factor. PLoS Pathog. 2011;7. doi:10.1371/journal.ppat.1002392

956 65. Grosche C, Diehl A, Rensing SA, Maier UG. Iron–sulfur cluster biosynthesis in algae with
957 complex plastids. Embley M, editor. Genome Biology and Evolution. 2018;10: 2061–2071.
958 doi:10.1093/gbe/evy156

959 66. Katoh K, Rozewicki J, Yamada KD. MAFFT online service: multiple sequence alignment,
960 interactive sequence choice and visualization. Briefings in Bioinformatics. 2019;20: 1160–1166.
961 doi:10.1093/bib/bbx108

962 67. Criscuolo A, Gribaldo S. BMGE (Block Mapping and Gathering with Entropy): a new software for
963 selection of phylogenetic informative regions from multiple sequence alignments. BMC Evol
964 Biol. 2010;10: 210. doi:10.1186/1471-2148-10-210

965 68. Trifinopoulos J, Nguyen L-T, von Haeseler A, Minh BQ. W-IQ-TREE: a fast online phylogenetic
966 tool for maximum likelihood analysis. Nucleic Acids Res. 2016;44: W232–W235.
967 doi:10.1093/nar/gkw256

968 69. Minh BQ, Nguyen MAT, Von Haeseler A. Ultrafast approximation for phylogenetic bootstrap.
969 Molecular Biology and Evolution. 2013;30: 1188–1195. doi:10.1093/molbev/mst024

970 70. Tamura K, Stecher G, Kumar S. MEGA11: Molecular Evolutionary Genetics Analysis version 11.
971 Battistuzzi FU, editor. Molecular Biology and Evolution. 2021;38: 3022–3027.
972 doi:10.1093/molbev/msab120

973 71. Letunic I, Bork P. Interactive Tree of Life (iTOL) v6: recent updates to the phylogenetic tree
974 display and annotation tool. Nucleic Acids Research. 2024;52: W78–W82.
975 doi:10.1093/nar/gkae268

976 72. Lévêque MF, Berry L, Cipriano MJ, Nguyen H-M, Striepen B, Besteiro S. Autophagy-related
977 protein ATG8 has a noncanonical function for apicoplast inheritance in Toxoplasma gondii.
978 MBio. 2015;6: e01446-15.

979 73. Nguyen HM, Liu S, Daher W, Tan F, Besteiro S. Characterisation of two Toxoplasma PROPPINs
980 homologous to Atg18/WIPI suggests they have evolved distinct specialised functions. PLoS ONE.
981 2018;13: e0195921. doi:10.1371/journal.pone.0195921

982 74. Kong-Hap MA, Mouammine A, Daher W, Berry L, Lebrun M, Dubremetz J-F, et al. Regulation of
983 ATG8 membrane association by ATG4 in the parasitic protist Toxoplasma gondii. Autophagy.
984 2013;9: 1334–1348. doi:10.4161/auto.25189

985 75. Anderson-White BR, Ivey FD, Cheng K, Szatanek T, Lorestani A, Beckers CJ, et al. A family of
986 intermediate filament-like proteins is sequentially assembled into the cytoskeleton of
987 Toxoplasma gondii. Cell Microbiol. 2011;13: 18–31. doi:10.1111/j.1462-5822.2010.01514.x

988 76. Couvreur G, Sadak A, Fortier B, Dubremetz JF. Surface antigens of Toxoplasma gondii.
989 Parasitology. 1988;97 (Pt 1): 1–10.

990 77. Herm-Gotz A. Toxoplasma gondii myosin A and its light chain: a fast, single-headed, plus-end-
991 directed motor. The EMBO Journal. 2002;21: 2149–2158. doi:10.1093/emboj/21.9.2149

992 78. Hajj HE, Lebrun M, Fourmaux MN, Vial H, Dubremetz JF. Characterization, biosynthesis and fate
993 of ROP7, a ROP2 related rhoptry protein of Toxoplasma gondii☆. Molecular and Biochemical
994 Parasitology. 2006;146: 98–100. doi:10.1016/j.molbiopara.2005.10.011

995 79. Crawford MJ, Thomsen-Zieger N, Ray M, Schachtner J, Roos DS, Seeber F. Toxoplasma gondii
996 scavenges host-derived lipoic acid despite its de novo synthesis in the apicoplast. EMBO J.
997 2006;25: 3214–3222. doi:10.1038/sj.emboj.7601189

998 80. Berger N, Vignols F, Przybyla-Toscano J, Roland M, Rofidal V, Touraine B, et al. Identification of
999 client iron–sulfur proteins of the chloroplastic NFU2 transfer protein in Arabidopsis thaliana.
1000 Takahashi H, editor. Journal of Experimental Botany. 2020;71: 4171–4187.
1001 doi:10.1093/jxb/eraa166

1002 81. Cox J, Mann M. MaxQuant enables high peptide identification rates, individualized p.p.b.-range
1003 mass accuracies and proteome-wide protein quantification. Nat Biotechnol. 2008;26: 1367–
1004 1372. doi:10.1038/nbt.1511

1005 82. Hehl AB, Basso WU, Lippuner C, Ramakrishnan C, Okoniewski M, Walker RA, et al. Asexual
1006 expansion of Toxoplasma gondii merozoites is distinct from tachyzoites and entails expression
1007 of non-overlapping gene families to attach, invade, and replicate within feline enterocytes.
1008 BMC Genomics. 2015;16: 66. doi:10.1186/s12864-015-1225-x

1009 83. Smyth GK. Linear models and empirical bayes methods for assessing differential expression in
1010 microarray experiments. Stat Appl Genet Mol Biol. 2004;3: Article3. doi:10.2202/1544-
1011 6115.1027

1012 84. Daniel Gietz R, Woods RA. Transformation of yeast by lithium acetate/single-stranded carrier
1013 DNA/polyethylene glycol method. Methods in Enzymology. Elsevier; 2002. pp. 87–96.
1014 doi:10.1016/S0076-6879(02)50957-5

1015 85. Semenovskaya K, Lévêque MF, Berry L, Bordat Y, Dubremetz J, Lebrun M, et al. TgZFP2 is a
1016 novel zinc finger protein involved in coordinating mitosis and budding in Toxoplasma. Cellular
1017 Microbiology. 2020;22: e13120.

1018 86. Henkel S, Frohnecke N, Maus D, McConville MJ, Laue M, Blume M, et al. Toxoplasma gondii
1019 apicoplast-resident ferredoxin is an essential electron transfer protein for the MEP isoprenoid-
1020 biosynthetic pathway. J Biol Chem. 2022;298: 101468. doi:10.1016/j.jbc.2021.101468

1021 87. Lamarque MH, Roques M, Kong-Hap M, Tonkin ML, Rugarabamu G, Marq J-B, et al. Plasticity
1022 and redundancy among AMA-RON pairs ensure host cell entry of Toxoplasma parasites. Nat
1023 Commun. 2014;5: 4098. doi:10.1038/ncomms5098

1024

1025 **Suppl. Table Legends**

1026 **S1 Table. Sequences used for the phylogenetic analysis displayed in Fig. 1A.** Abbreviations used in
1027 the Fig. 1A phylogenetic analysis are mentioned in red next to each sequence.

1028 **S2 Table. Proteins with higher expression upon depletion of TgHCF101 as found by label-free**
1029 **quantitative proteomics.** For each protein candidate (with www.ToxoDB.org and www.Uniprot.org
1030 identifier), $\log_2$ of the different ratio were calculated between the mean MaxQuant LFQ values found
1031 for the cKD HA-TgHCF101 mutant and the TATi ΔKu80 parental cell line. $-\log_{10}$(pvalue) is also provided.
1032 Putative subcellular localization was obtained from the hyperLOPIT data available on ToxoDB.org, or
1033 by manual annotation. CRISPR fitness score and transcriptomic data for tachyzoites (Tz) and
1034 bradyzoites (Bz) were obtained from ToxoDB.org.

1035 **S3 Table. Proteins with lower expression upon depletion of TgHCF101 as found by label-free**
1036 **quantitative proteomics.** For each protein candidate (with www.ToxoDB.org and www.Uniprot.org
1037 identifier), $\log_2$ of the different ratio were calculated between the mean MaxQuant LFQ values found
1038 for the cKD HA-TgHCF101 mutant and the TATi ΔKu80 parental cell line. $-\log_{10}$(pvalue) is also provided.
1039 Putative subcellular localization was obtained from the hyperLOPIT data available on ToxoDB.org, or
1040 by manual annotation. CRISPR fitness score and transcriptomic data for tachyzoites (Tz) and
1041 bradyzoites (Bz) were obtained from ToxoDB.org.

1042 **S4 Table. Proteins identified as co-immunoprecipitating with TgHCF101 through comparative mass**
1043 **spectrometry analysis of immunoprecipitated extracts form the cKD HA-TgHCF101 cell line grown or**
1044 **not in the presence of ATc.** Proteins enriched (TgHCF101-expressing sample vs TgHCF101-depleted
1045 control) in a statistically significant way (p-value ≤ 0.05, and Benjamini-Hochberg correctin) are in green
1046 (dark green for TgHCF101 and putative iron-sulfur protein) and those less abundant are in red.

1047

1048 **S5 Table. Oligonucleotides used in this study.**

1049

1050 **Figure 1**

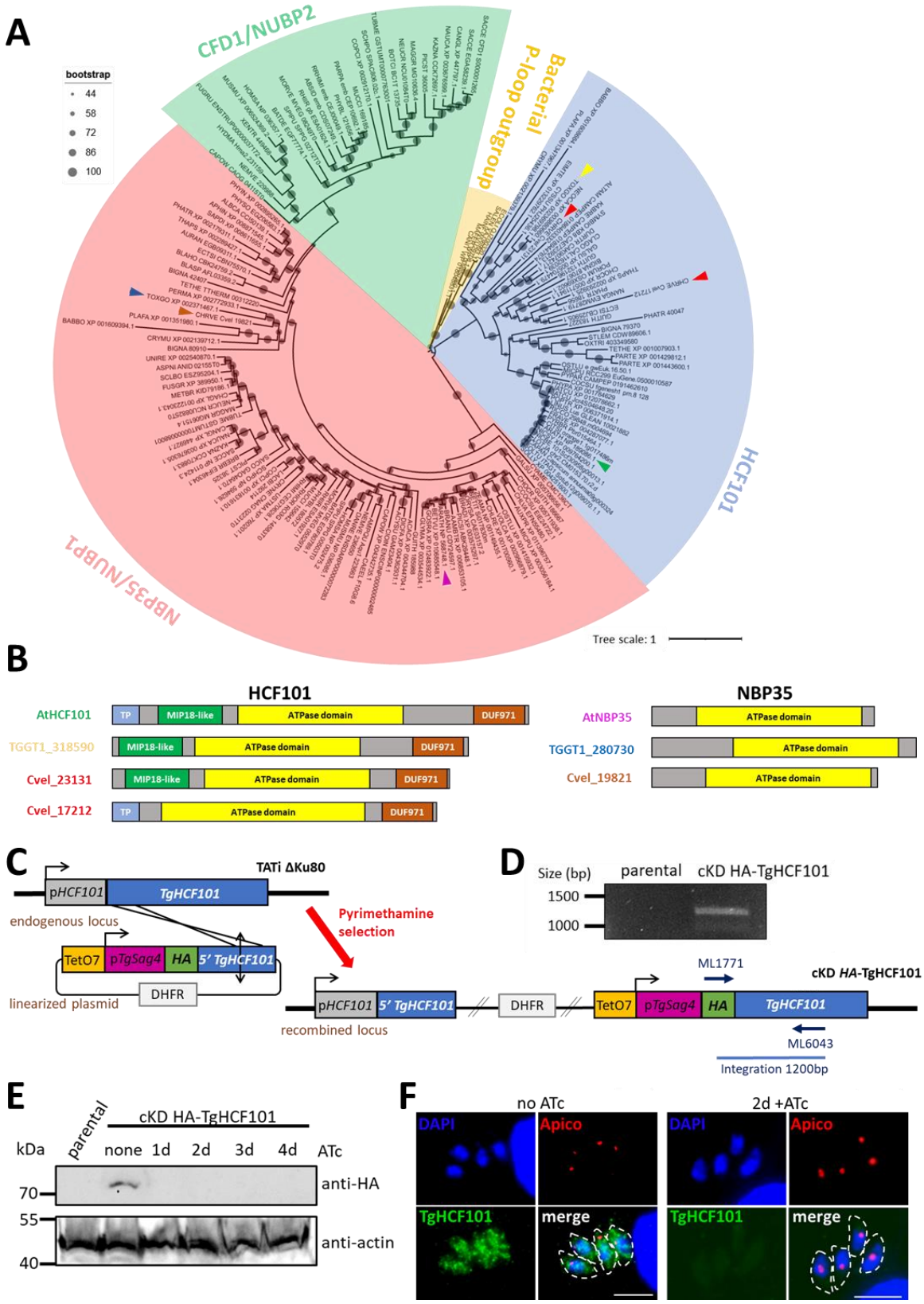

1051

1052 **Figure 1. TgHCF101 is a cytosolic protein. A.** Evolutionary relationship of proteins of the MRP family.
1053 Eukaryotic sequences from HCF101 homologs were aligned and submitted to phylogenetic analysis

1054 with the maximum likelihood method. Scale bar represents 1 residue substitution per site. Bacterial P-
1055 loop ATPase sequences were used as an outgroup. HCF101 from *A. thaliana* is indicated by a green
1056 arrowhead, TgHCF101 by a yellow arrowhead and the two homologs present in *C. velia* are indicated
1057 by red arrowheads. NBP35 homologs from *A. thaliana, T. gondii* and *C. velia* are indicated by purple,
1058 blue and brown arrowheads, respectively. **B.** Schematic representation of homologs for HCF101 in *A.*
1059 *thaliana* (AtHCF101), in *T. gondii* (TGGT1_318590) and in *C. velia* (Cvel_23131, Cvel_17212), and
1060 homologs for NBP35 in *A. thaliana* (AtNBP35), in *T. gondii* (TGGT1_280730) and in *C. velia*
1061 (Cvel_19821). Main domains are highlighted on the sequences; TP: predicted transit peptide, MIP18-
1062 like domain (or Domain of unknown function 59, DUF59), the ATPase domain and DUF971. **C.** Strategy
1063 for generating the inducible knockdown of *TgHCF101* by promoter replacement and simultaneous N-
1064 terminal tagging of the TgHCF101 protein in the TATi ΔKu80 cell line. **D.** Diagnostic PCR for checking
1065 correct integration using the primers mentioned in (B), on genomic DNAs of a transgenic parasite clone
1066 and of the parental strain. **E.** Immunoblot analysis of the cKD-TgHCF101 mutant and parental line
1067 showing efficient tagging and downregulation of TgHCF101 starting at 24h of treatment with ATc. Actin
1068 was used as a loading control. **F.** Immunofluorescence assay showing a cytosolic signal for TgHCF101
1069 protein (labeled with an anti-HA antibody), with no particular co-localization with the apicoplast
1070 (Apico, labeled with anti-PDH-E2 antibody), and total depletion of the protein after 48h of ATc
1071 treatment. DNA was stained with 4',6-diamidino-2-phenylindole (DAPI). Scale bar= 5 µm.

1072

1073 **Figure 2**

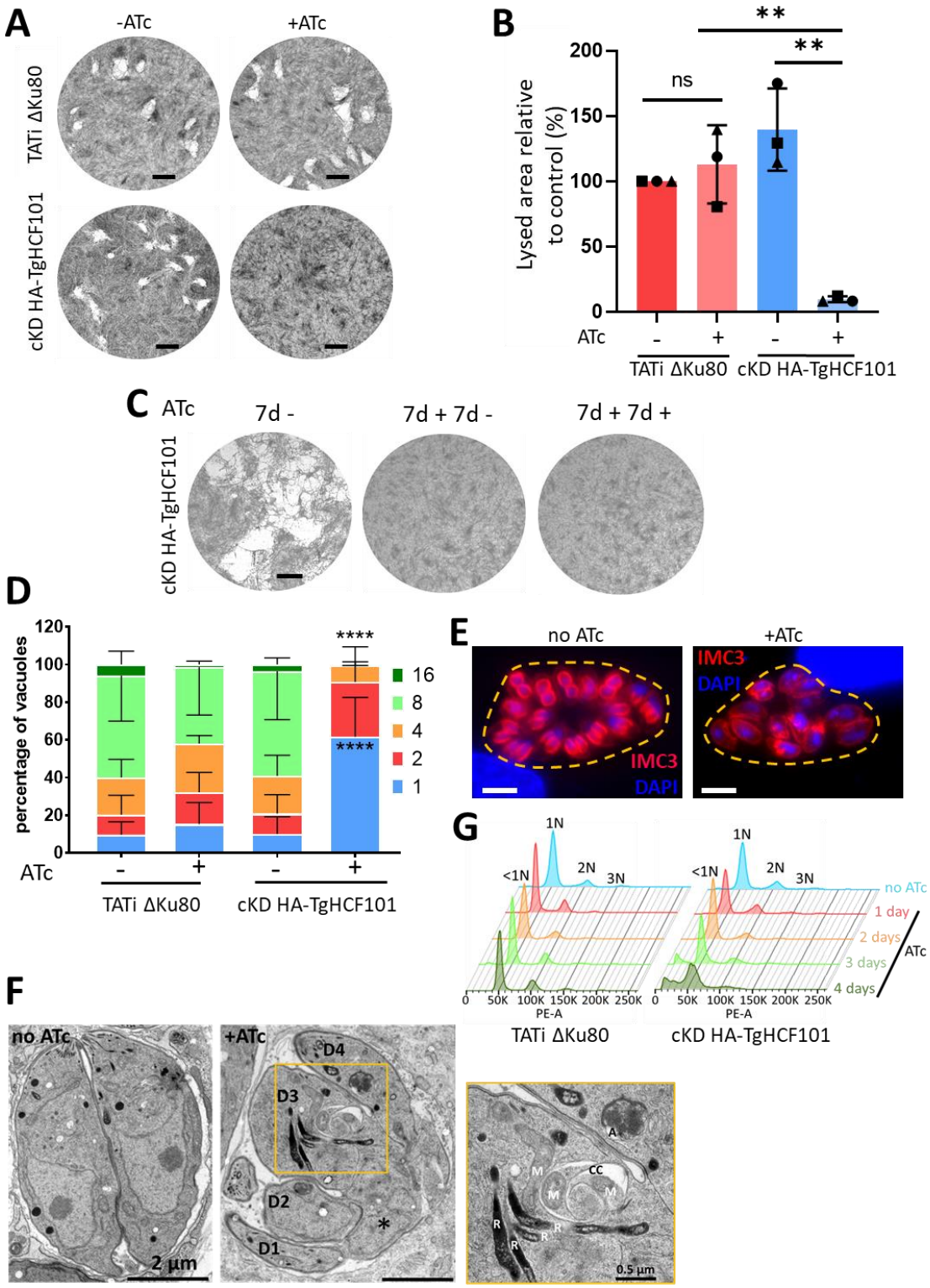

1074

1075 **Figure 2. TgHCF101 is essential for parasite growth and survival. A.** Plaque assays were carried out by
1076 infecting a monolayer of HFFs with TATi ΔKu80 or cKD-TgHCF101 cell lines for 7 days in the presence
1077 or absence of ATc. Scale bar= 2 mm. **B.** Quantification of plaque area observed in (A). Results are
1078 expressed as percentage of lysed area relative to control (TATi ΔKu80 -ATc, set as 100% for reference).
1079 Values represented are mean ± SD from n=3 independent biological replicates, ** p-value ≤ 0.01,
1080 Student *t*-test **C.** Plaque assays were carried out with cKD-TgHCF101 parasites as described in (A) but

1081 for the ‘7d+7d-‘ condition, ATc was washed-out after 7 days and parasites were allowed to grow for
1082 another 7 days without ATc, while in the ‘7d+7d+’ condition, ATc treatment was maintained for 7 more
1083 days. The ‘7d –‘ control was kept without ATc for 7 days of growth. Scale bar= 2mm. **D.** Replication
1084 assay of parental (TATi ΔKu80) and transgenic cell lines (cKD-TgHCF101): parasites were pre-cultured
1085 for 48h in the presence or absence of ATc and allowed to invade HFF-coated coverslips for another 24h
1086 in the presence or absence of ATc, for a total of up to 72h of treatment with ATc. Number of parasites
1087 per vacuole was quantified for each condition and expressed as a percentage, 200 vacuoles were
1088 counted for each condition. Values represented are mean ± SD of 3 independent biological replicates,
1089 **** p-value ≤ 0.0001 by two-way ANOVA with Dunnett’s multiple comparison test, showing a
1090 significant difference when comparing the TATi ΔKu80 control and cKD-TgHCF101+ATc parasites for
1091 percentage of vacuoles containing 1 or 8 parasites. **E.** DNA content analysis by flow cytometry on TATi
1092 ΔKu80 and cKD-TgHCF101 parasites treated or not with ATc up to 4 days and stained with propidium
1093 iodide. 1N, 2N, 3N represent the ploidy, with <1N corresponding to parasites with less than 1 full
1094 nuclear DNA content. **F.** Immunofluorescence assay of cKD-TgHCF101 parasites showing asynchronous
1095 division of parasites growing in the same vacuole (outlined with a yellow dotted line) upon TgHCF101
1096 depletion (+ATc condition: parasites pre-incubated for 48h with ATc and allowed to invade coverslips
1097 for another 48h in the presence of ATc). Individual parasites and budding daughter cells are outlined
1098 by anti-IMC3 antibody staining (magenta), DNA was stained with DAPI. Scale bar= 5 µm. **G.** Electron
1099 microscopy of cKD-TgHCF101 parasites pre-incubated with ATc for 24h before being released from
1100 their host cell and allowed to reinvade for 24h in the presence (+ATc) or grown in absence of ATc (-
1101 ATc). D: daughter bud, R: rhoptry, A: apicoplast, M: mitochondrion, CC: cytoplasmic cleft. The asterisk
1102 denotes unincorporated nuclear material. Scale bar= 2 µm (0.5 µM for inset magnification).

1103

1104 **Figure 3**

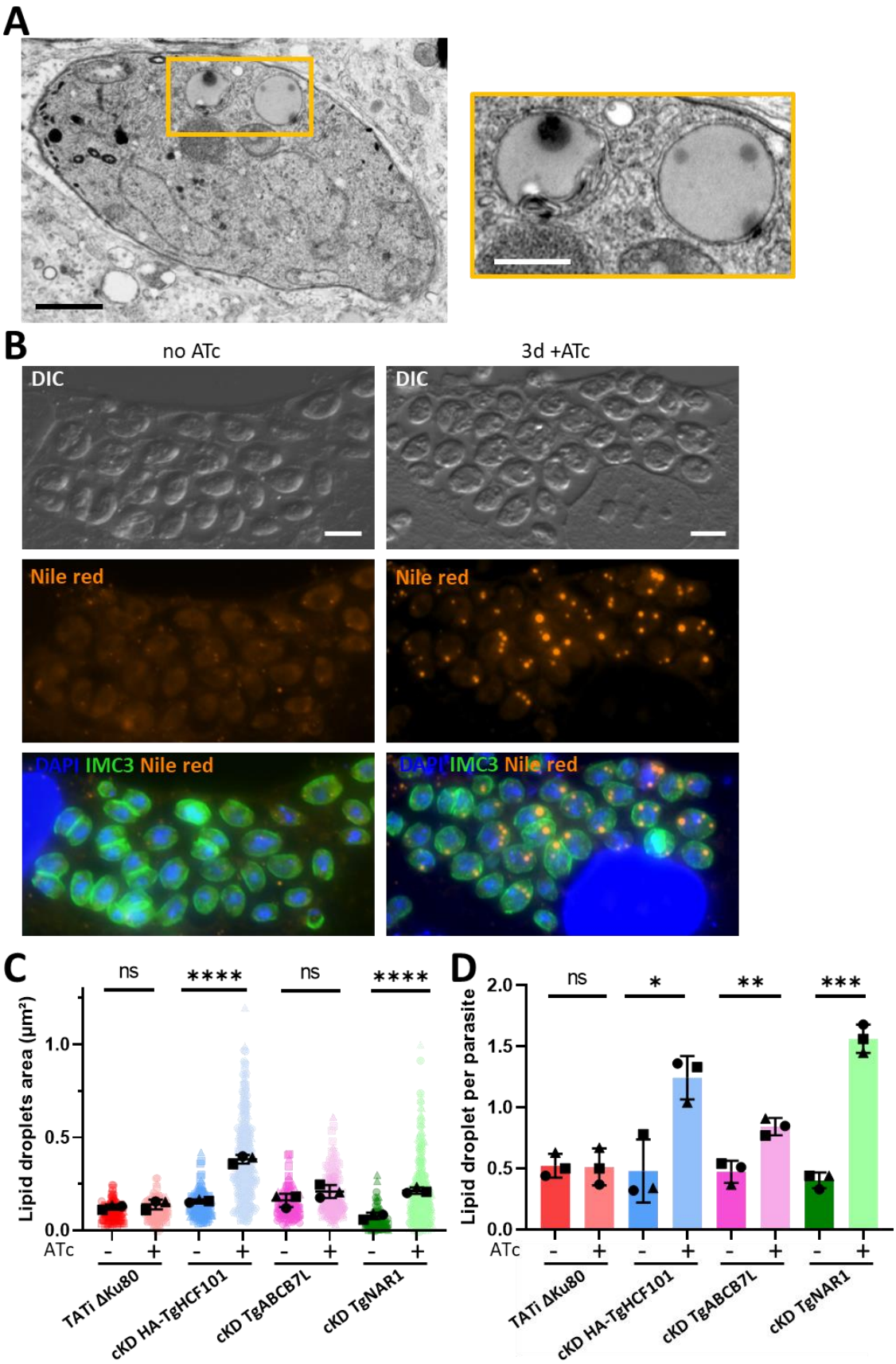

1105

1106 **Figure 3. TgHCF101 depletion induces lipid droplet accumulation. A.** Electron microscopy of cKD-
1107 TgHCF101 parasites pre-incubated with ATc for 48h and allowed to reinvade for 24h in the presence
1108 of ATc. Scale bar= 1 µm. The panel on the right corresponds to a magnification of the selection on the
1109 left panel, highlighting lipid droplets. Scale bar= 500 nm **B.** Fluorescent imaging of parasites from the
1110 cKD-TgHCF101 cell line treated for 72h with ATc or in grown the absence of ATc, shows an
1111 accumulation of lipid droplets upon TgHCF101 depletion. Lipid droplets were detected with Nile red
1112 (orange), parasites are outlined with an anti-IMC3 antibody (green) and DNA is stained with DAPI. DIC=
1113 Differential interference contrast. Scale bar= 5 µm. **C.** and **D.** correspond to the quantification of lipid
1114 droplet area and number, respectively. 100 parasites were analyzed per condition. The parental (TATi
1115 ΔKu80) and transgenic parasites (cKD HA-TgHCF101, cKD TgABCB7, cKD TgNAR1) were grown in
1116 absence of ATc, or in presence of ATc for 72h. Values are represented as the mean ± SD of n=3
1117 independent biological replicates (different symbols represent different series); ns, not significant (p-
1118 value>0.05), * p-value ≤ 0.05, ** p-value ≤ 0.01, *** p-value ≤ 0.001, **** p-value ≤ 0.0001, Student's
1119 *t*-test.

1120

1121 **Figure 4**

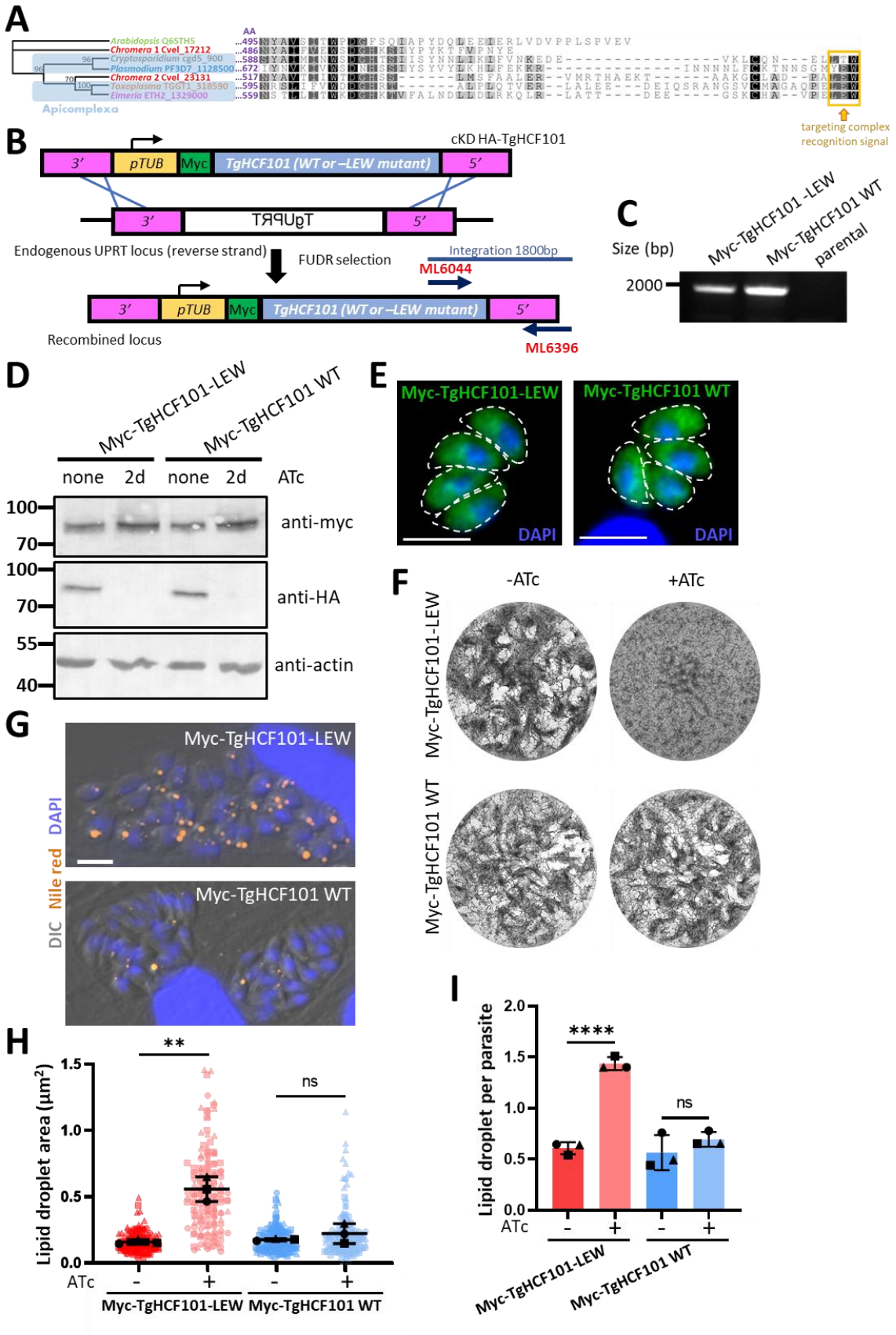

1122

1123 **Figure 4. A C-terminal TCR-like motif is necessary for TgHCF101 function. A**. Alignment of the C-
1124 terminal region of HCF101 homologs from different eukaryotes, including the plant *A. thaliana*, the
1125 two isoforms of Apicomplexa-relative photosynthetic algae *C. velia*, as well as several Apicomplexa
1126 species (*T. gondii*, *Eimeria tenella*, *P. falciparum* and apicoplast-less *Cryptosporidium parvum*). The
1127 tryptophan-containing targeting complex recognition (TCR) signal is highlighted in yellow. Consensus
1128 tree was obtained with protein alignment and bootstrap values (500 replicates) are indicated at the
1129 base of the nodes. **B.** Schematic representation of the strategy for generating cell lines expressing myc-
1130 tagged wild-type (WT) or TCR motif-deleted (-LEW) copies of TgHCF101 by integrating an extra copy of
1131 the gene of interest by double homologous recombination at the *Uracil Phosphoribosyltransferase*
1132 (*UPRT*) locus. Negative selection with 5-fluorodeoxyuridine (FUDR) was used to select transgenic
1133 parasites based on their absence of UPRT expression. **C.** Diagnostic PCR for verifying integration at the
1134 *UPRT* locus thanks to the primers described in **A. D.** Immunoblot analysis showing expression of the
1135 additional myc-tagged copies upon depletion of the ATc-regulated HA-tagged copy. **E.**
1136 Immunofluorescence with anti-myc antibody confirms the cytoplasmic localization of the extra copies.
1137 Parasite shape is outlined. DNA was stained with DAPI. Scale bar= 5 µm. **F.** Plaque assay showing
1138 restoration of growth by the additional WT copy upon depletion of the ATc-regulated copy, contrarily
1139 to the TCR mutant. **G.** Representative images of vacuoles (outlined) containing parasites grown
1140 continuously in the presence of ATc for 72 hours and stained by Nile red (orange) for lipid droplets.
1141 DIC: differential interference contrast. DNA was stained with DAPI. Scale bar= 10 µm. **H.** and **I.**
1142 correspond to the quantification of lipid droplet area and number, respectively. 100 parasites were
1143 analyzed per condition. WT or TCR-depleted (-LEW) parasites were grown in presence of ATc for 72h.
1144 Values are represented as the mean ± SD of n=3 independent biological replicates (different symbols
1145 represent different series); ns, not significant (p-value>0.05), ** p-value ≤ 0.01, **** p-value ≤ 0.0001,
1146 Student's *t*-test.

1147

1148 **Figure 5**

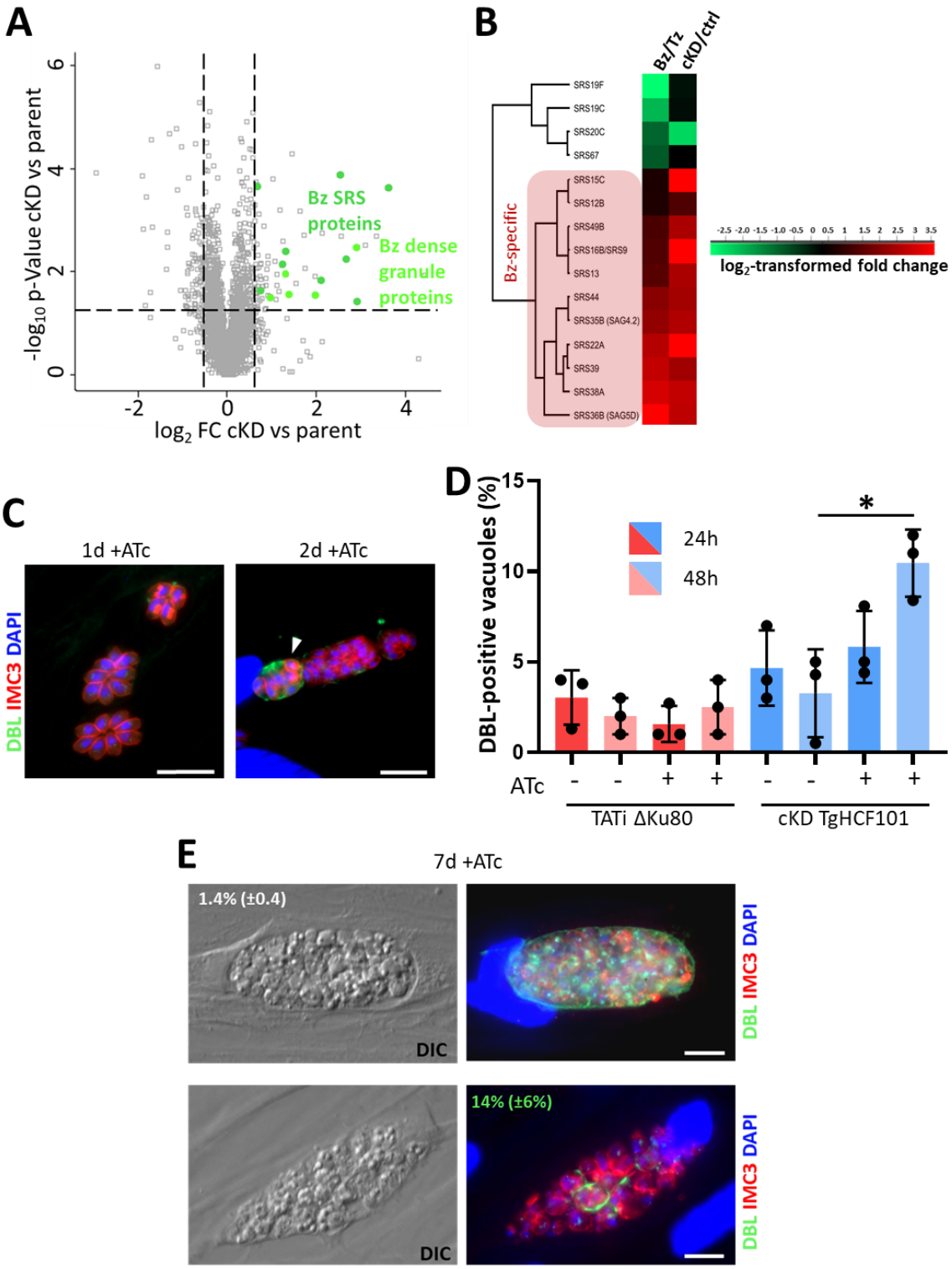

1149

1150 **Figure 5. TgHCF101-depleted parasites express bradyzoite-specific markers but are unable to**
1151 **complete their conversion. A.** Volcano plot showing differential expression of proteins impacted by
1152 TgHCF101 depletion after 72h of ATc treatment analyzed by label free quantitative proteomic. X-axis
1153 corresponds to the $\log_2$ of the fold-change (FC) and the Y-axis corresponds to the $-\log_{10}$ of the p-value,
1154 when comparing cKD-TgHCF101 expression values to the TATi ΔKu80 parental cell line. Statistical

1155 analyses were performed with ANOVA on 4 independent biological replicates. Cut-offs were set at
1156 ≤1.5- or ≥1.5-FC and p-value ≤0.05. Significant hits corresponding to stage-specific protein are
1157 highlighted in green on the graph. **B.** Clustering of bradyzoite (Bz) or tachyzoite (Tz)-specific proteins
1158 of the SRS family shows specific enrichment of bradyzoite proteins upon TgHCF101 depletion. **C.**
1159 Immunofluorescence assay of cKD-TgHCF101 treated for 24h or 48h with ATc, cyst wall is labeled with
1160 DBL, parasites periphery is outlined with anti-IMC3 antibody and DNA is stained with DAPI. Scale bar=
1161 10µm **D.** Corresponds to the quantification of the percentage of vacuoles presenting a DBL positive
1162 signal as shown in (C). Values are represented as the mean ± SD of n=3 independent biological
1163 replicates, * p-value ≤ 0.05, Student's *t*-test. **E.** Immunofluorescence assay of cKD-TgHCF101 treated
1164 for 7 days in the presence of ATc, cyst wall is labeled with DBL, parasites are outlined with anti-IMC3
1165 antibody and DNA is stained with DAPI. The percentage of DBL positive vacuoles of corresponding size
1166 (more than 2 parasites per vacuole, top; or 2 parasites per vacuole or less, bottom) is specified as mean
1167 ± SD of n=3 independent biological replicates. DIC= Differential interference contrast. Scale bar= 10
1168 µm.

1169

1170 **Figure 6**

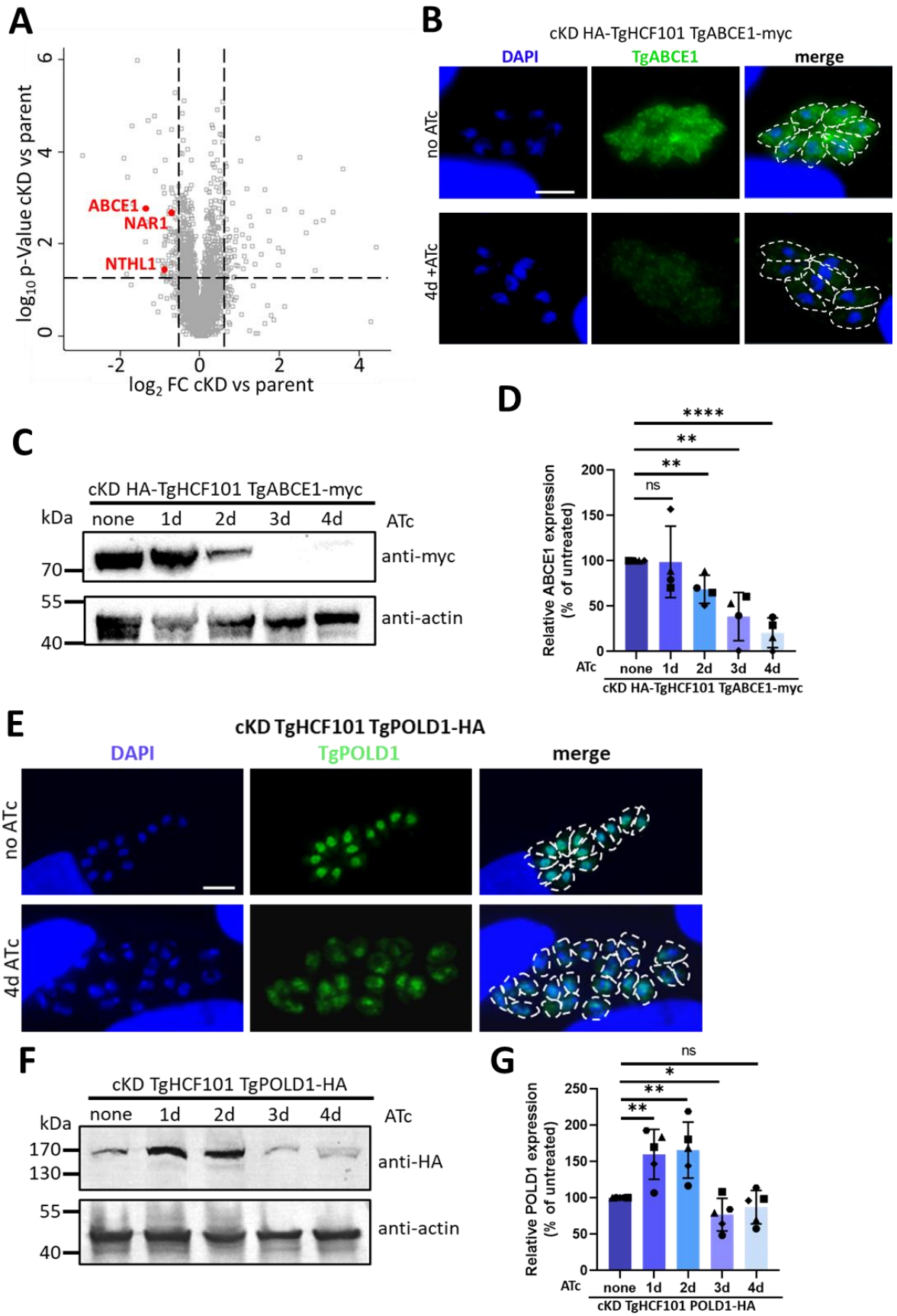

1171

1172 **Figure 6. TgHCF101 is involved in Fe-S cluster biogenesis of the CIA pathway. A.** Volcano plot showing
1173 differential expression of proteins impacted by TgHCF101 depletion after 72h of ATc treatment
1174 analyzed by label free quantitative proteomic. Cut-offs were set at ≤1.5- or ≥1.5-fold change (FC) and
1175 p-value ≤0.05. Significant hits corresponding to predicted Fe-S cluster proteins are highlighted in red
1176 on the graph. **B.** Immunofluorescence assay for the detection of myc-tagged TgABCE1 in the cKD
1177 TgHCF101 genetic background. Parasites were pre-incubated for 48h in the presence of ATc and
1178 allowed to invade HFF coated coverslips for another 48h in the presence of ATc. The control (no ATc)
1179 was infected 24h prior to fixation. TgABCE1 was detected with an anti-myc antibody and DNA was
1180 stained with DAPI. Parasites periphery is outlined by white dotted lines. Scale bar=5 µm. **C.** Immunoblot
1181 analysis of TgABCE1 abundance shows decrease upon TgHCF101 depletion following up to 4 days of
1182 treatment with ATc of the cKD HA-TgHCF101 TgABCE1-myc cell line. TgABCE1 was detected with anti-
1183 myc antibody and anti-actin antibody was used as a loading control. **D.** Decrease of TgABCE1
1184 expression upon TgHCF101 depletion was quantified by band densitometry analysis and normalized
1185 on the loading control of each respective lane. The relative abundance of TgABCE1 is presented as a
1186 percentage relative to the untreated control, set as 100%, for each biological replicate. Values are
1187 represented as the mean ± SD from n=4 independent biological replicates, ** p-value ≤ 0.01, **** p-
1188 value ≤ 0.0001; ns, not significant (p-value ≥ 0.05), Student's *t*-test. **E.** Immunofluorescence assay for
1189 the detection of HA-tagged TgPOLD1 in the cKD TgHCF101 genetic background. Parasites were pre-
1190 incubated for up to four days in presence of ATc on HFF-coated coverslips. The control (no ATc) was
1191 infected 24h prior to fixation. TgPOLD1 was detected with an anti-HA antibody and DNA was stained
1192 with DAPI. Parasites periphery is outlined by white dotted lines. Scale bar=5 µm. **F.** Immunoblot
1193 analysis of TgPOLD1 abundance in conditions of TgHCF101 depletion following up to 4 days of
1194 treatment with ATc of the cKD TgHCF101 TgPOLD1-HA cell line. TgPOLD1 expression was detected with
1195 anti-HA antibody and anti-actin antibody was used as a loading control. **G.** Changes in TgPOLD1
1196 expression upon TgHCF101 depletion was quantified by band densitometry analysis and normalized
1197 on the loading control of each respective lane. The relative abundance of TgPOLD1 is presented as a
1198 percentage relative to the untreated control, set as 100%, for each biological replicate. Values are
1199 represented as the mean ± SD from n=5 independent biological replicates, * p-value ≤ 0.05; ** p-value
1200 ≤ 0.01; ns, not significant (p-value ≥ 0.05), Student's *t*-test.

1201

1202 **Figure 7**

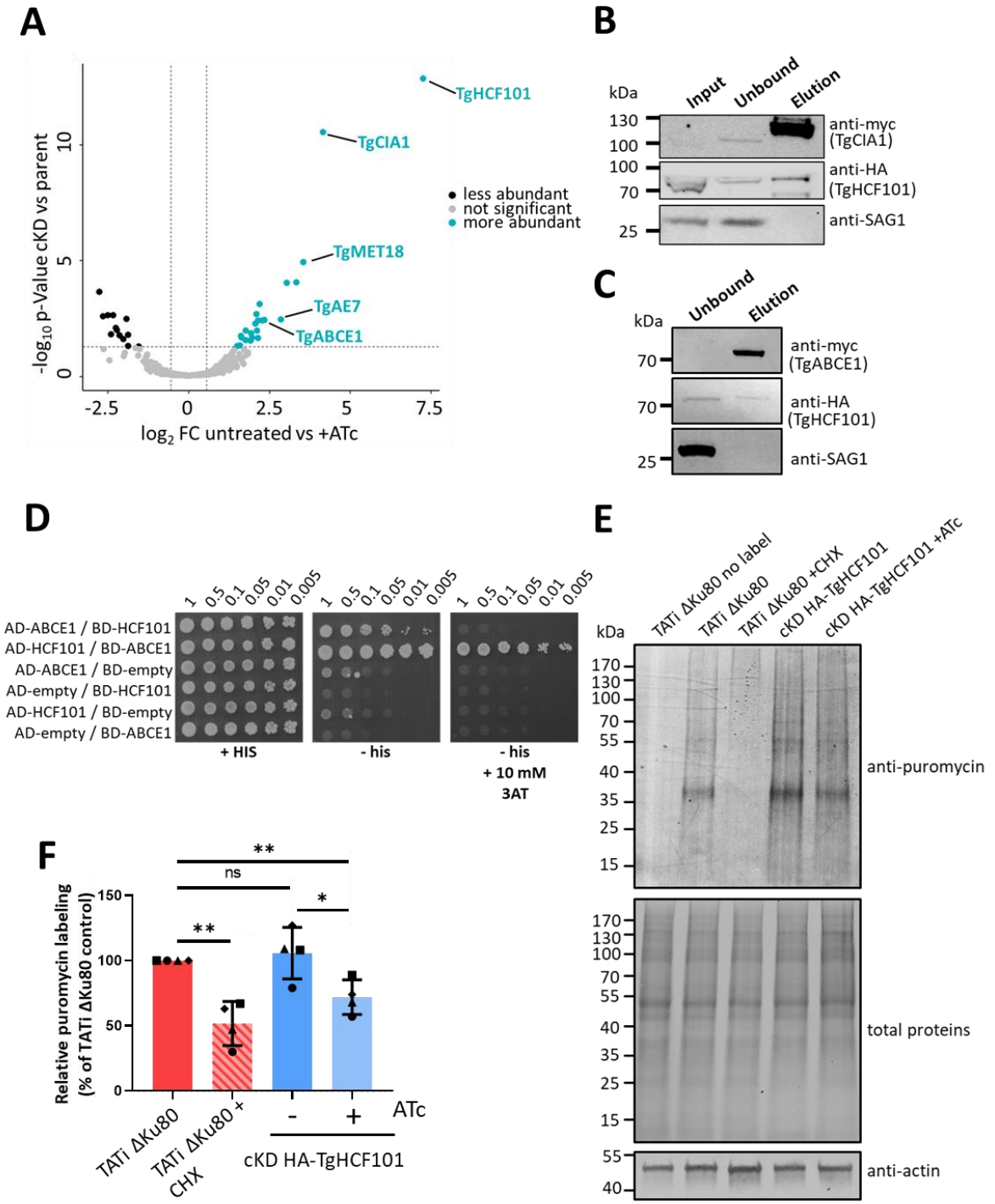

1203

1204 **Figure 7. TgHCF101 is associated to the CIA targeting complex and specifically interacts with**
1205 **TgABCE1. A.** Volcano plot showing differential expression of TgHCF101 and co-immunoprecipitated
1206 proteins in the cKD HA-TgHCF101 cell line after TgHCF101 depletion (with 72h of ATc treatment) or
1207 not, as analyzed by quantitative proteomic. Cut-offs were set at ≤1.5- or ≥1.5-fold change and p-value
1208 ≤0.05. Upregulated proteins are highlighted in blue, significant hits corresponding to predicted
1209 proteins of the CIA targeting complex and target protein TgABCE1 were annotated on the graph. **B.**
1210 Immunoblot analysis of a reverse co-immunoprecipitation assay of the myc-tagged TgCIA1 protein in
1211 the cKD HA-TgHCF101 background shows specific co-immunoprecipitation of TgHCF101, which is

1212 absent upon depletion by ATc. The anti-SAG1 antibody was used as a control for unspecifically bound
1213 proteins. **C.** Immunoblot analysis of a reverse co-immunoprecipitation assay of the myc-tagged
1214 TgABCE1 protein showing TgHCF101 is co-immunoprecipitating. The anti-SAG1 antibody was used as
1215 a control for unspecifically bound proteins. **D.** TgHCF101 interacts with TgABCE1 in a Gal4-based yeast
1216 two-hybrid assay. YRG2 cells co-transformed with AD- and BD-fusion proteins were grown to stationary
1217 phase, then serially diluted to OD_{600} values ranging from 1 to 5 x 10^{-3} before being spotted onto a
1218 control plate (+His, upper panel) to assess cell viability, and a Y2H test plate (-His, middle panel) to
1219 assess interaction. Plates were incubated at 30°C, and yeast growth was recorded after 5 days. As
1220 shown in the middle panel, TgHCF101 exhibited a strong interaction with TgABCE1, independent of
1221 cloning orientation. The strongest interaction was observed between AD-TgHCF101 and BD-TgABCE1,
1222 with co-transformed cells growing at the lowest dilution tested in the presence of 10 mM 3-
1223 aminotriazole (3AT) as a competitive inhibitor. Neither TgHCF101 nor TgABCE1 alone showed HIS3
1224 transactivation in the presence of 3AT. These results are representative of 3 independent experiments.
1225 **E.** Immunoblot analysis of puromycin incorporation in the parental (TATi ΔKu80) and cKD TgHCF101
1226 cell lines untreated or treated with ATc for 72h. TATi ΔKu80 treated with cycloheximide (CHX) was used
1227 as a control for translation inhibition. The puromycin signal was detected with anti-puromycin
1228 antibody, and total protein content was visualized by stain-Free imaging technology. Anti-actin
1229 antibody was also used as a loading control. **F.** Variation of puromycin incorporation in the different
1230 conditions was quantified by band densitometry and normalized on the total protein content of each
1231 respective lane. Puromycin labeling is presented as a percentage relative to the untreated control, set
1232 as 100% for each biological replicate. Values are represented as the mean and SD of 4 independent
1233 biological replicates; * p-value ≤ 0.05; ** p-value ≤ 0.01; ns, not significant (p-value ≥ 0.05), Student's
1234 *t*-test.

1235

1236

1237 **Figure 8**

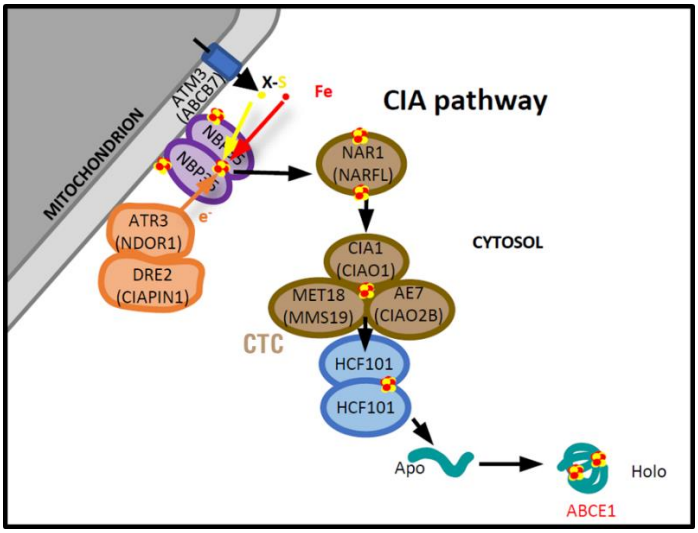

1238

1239 **Figure 8. Schematic representation of the putative organization of the CIA pathway in *T. gondii.*** This
1240 scheme places TgHCF101 as a Fe-S transfer protein from the CIA targeting complex (CTC) to client
1241 protein ABCE1. Plant nomenclature was used for the purpose of the figure, but names for human
1242 homologs are mentioned between brackets when appropriate.

1243